BiI_3: A Lower Toxicity Route to Tandem Solar Cells

Brian W. Williamson

A thesis

submitted in partial fulfillment of the

requirements for the degree of

Master of Science in Chemical Engineering

University of Washington

2017

Committee:

Hugh W. Hillhouse

Jim Pfaendtner

Program Authorized to Offer Degree:

Chemical Engineering

University of Washington

Abstract

BiI_3: A Lower Toxicity Route to Tandem Solar Cells

Brian W. Williamson

Chair of the Supervisory Committee:

Professor Hugh W. Hillhouse

Chemical Engineering

Global population is expected to grow by more than 2 billion people by mid-century. This will result in a large increase in electricity demand. However, any efforts in increasing electricity generation must take into account the health and environmental risks presented by traditional carbon-based fuel sources. Emphasis must be placed on generating electricity from zero-emission sources in an effort to mitigate the effects of climate change. Photovoltaic (PV) electricity generation is one such zero-emission generation method. Highly efficient, cheap, and low toxicity PV materials will be required to address this. In this work, we present an exploration of BiI_3 as a solution-processed, lower toxicity PV material. We show that BiI_3 films with 1 eV quasi-Fermi level splitting can be obtained from optimal processing conditions. We also explore how and why the different processing conditions influence morphology and optoelectronic quality of BiI_3 films. Finally, we discuss some of the limiting factors on achieving high efficiency BiI_3 devices.

Table of Contents

Chapter 1. Introduction

1.1 Global Energy Needs and Climate Change

Global population is projected to grow from 7 billon people in 2012 to 9 billion people by 2040.[1] Over the same period, global electricity consumption is projected to grow by 48%, from 18 TW to 27 TW.[2] Historically, we have met the majority of our energy generation needs via carbon-based sources, such as gasoline or natural gas. However, the environmental and health costs of using carbon-based fuels for the majority of our energy needs mean we must look for alternative energy sources. Anthropogenic temperature increases will result in accelerating sea level increases and changes to crop growing seasons.[3] This will in turn result in the displacement of populations around the world as they seek to escape these effects. Renewable energy sources such as wind and solar energy produce zero emissions and are a route to moving away from carbon-based energy productions. Solar energy production is especially attractive the estimated practically available energy is more than 20 times greater (600-1000 TW[4]) than the 2040 projected global electricity consumption.

1.2 Collecting Energy from the Sun

Solar panels function by absorbing sunlight and directly converting it to electricity. A typical solar cell is composed of front and back contacts, a base absorber layer, and an emitter layer (Figure 1). The defining feature for light absorption is the band gap (E_g) of the base layer. Band gap refers to the region in a material where no energy levels exist. When photons with energy (E) > E_g strikes the base layer, it is absorbed, creating an electron-hole pair. The separation of the electron-hole pair across the band gap creates a potential difference that can be used to do electrical work.[5]

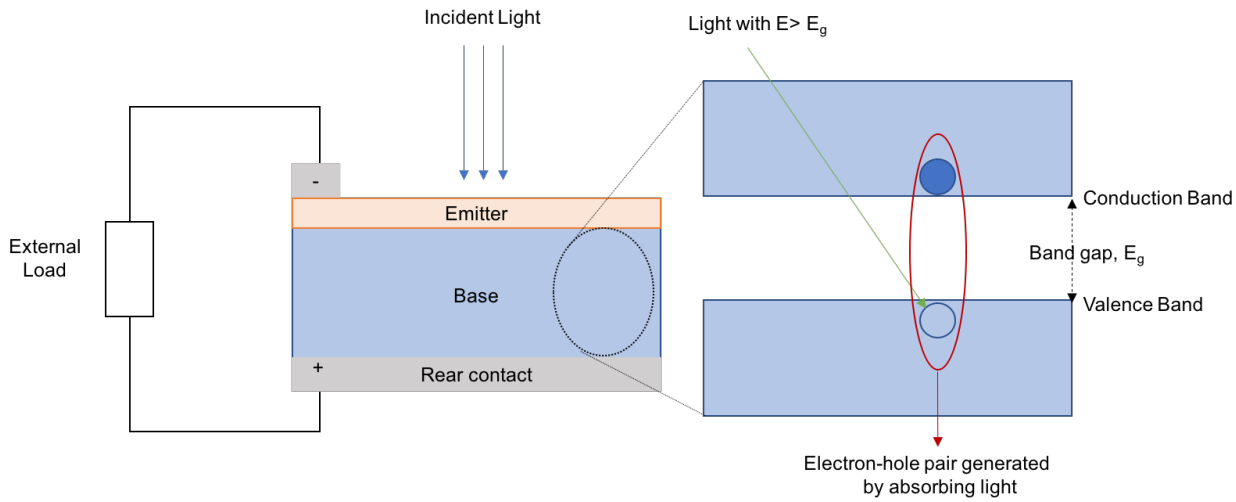

Figure 1. (Left) Schematic representation of a typical solar cell and (Right) the band gap of the absorber layer.

A solar cell made from a single light absorbing material will utilize photons slightly greater than the band gap energy most efficiently. Photons with $E < E_g$ will not be absorbed. Photons with $E >> E_g$ will be absorbed and promote an electron deeper into the conduction band, but the excited carrier will thermalize down to the band edge, meaning the extra energy is lost.[6] One way to resolve the issue of not using photons with $E >> E_g$ efficiently is to create what is called a tandem solar cell.

1.3 Tandem Solar Cells

Tandem or multi-junction solar cells utilize materials with complementary band gaps to efficiently harvest photons across a greater energy range. In a tandem configuration, a high band gap cell is placed on top of a lower band gap bottom cell (Figure 2). This allows the higher energy photons to be more efficiently used in the top cell, while allowing the lower energy photons to pass through to the bottom cell. A two-junction tandem solar cell increases the maximum theoretical efficiency from 30% for a single junction to 42%.[7] By coupling efficiency increases

from tandem cell architectures with low-cost manufacturing, it is possible to drive greater adaptation of solar energy across the world.

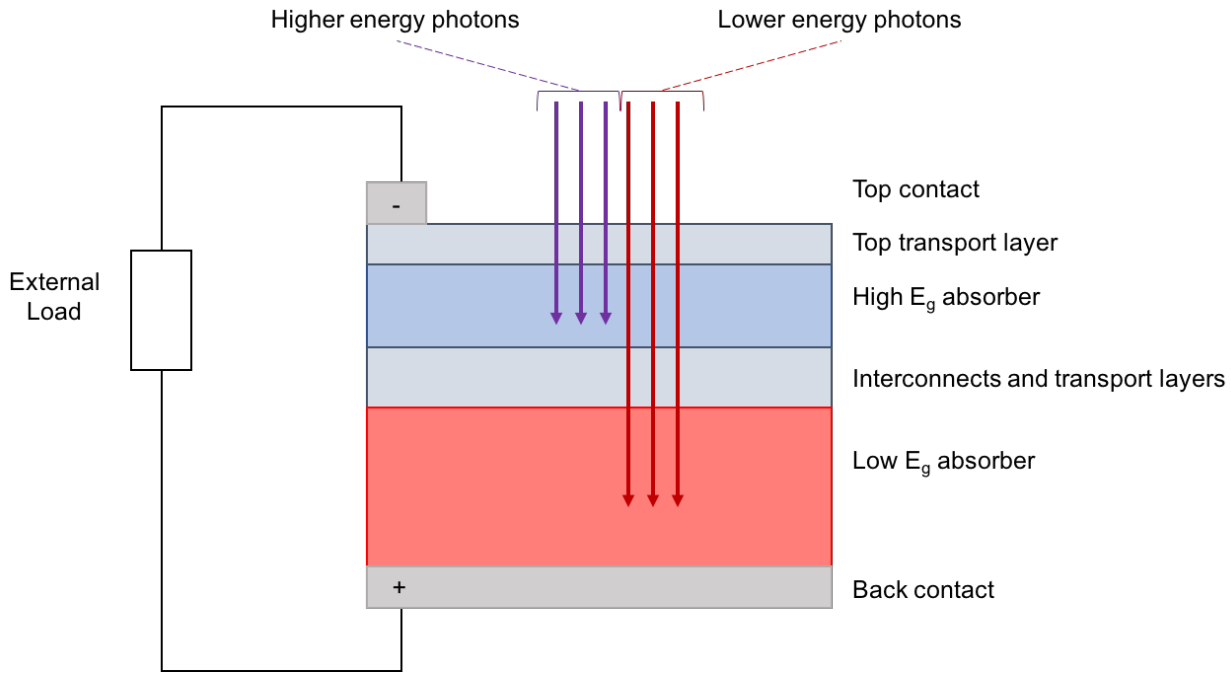

Figure 2: Schematic of a simple, two-junction tandem solar cell.

Chapter 2. Solution Processed BiI_3 Films with 1 eV Quasi-Fermi Level Splitting: Role of Water, Temperature, and Solvent During Processing

The following is an original article, reproduced in its entirety.

2.1 Solution Processed Photovoltaic Materials and BiI_3

Photovoltaic (PV) materials such as copper zinc tin sulfoselenide (CZTS)[8-10], copper indium gallium sulfoselenide (CIGS)[11-13], and more recently, hybrid perovskites (HPs)[14-16] are all solution processable. Solution processed materials are exciting since they can be spray coated, blade coated, or slot die coated onto large substrates, often at low temperature,[17] and thus may reduce the upfront capital expenditure to begin manufacturing (CAPEX).[18]The CAPEX of roll-to-roll processing is

0.06 \$/W_p versus 0.68 to 1.01 \$/W_p for CdTe and silicon processes. However, materials such as CZTS are not yet commercializable as device efficiencies are still less than 15% mainly due to low minority carrier diffusion lengths.[19] However, CIGS cells are commercial and have demonstrated module efficiencies of 16.5% for vacuum-deposited absorbers.[20] Solution processed CIGS is also being developed with lab-scale efficiencies of 14.7%.[13] The process still requires a high-temperature step, and indium (used in CIGS) is considered by some to add financial risk due to indium price volatility or constraints on the manufacturing growth rate.[21] Solution processed HP efficiencies have increased rapidly and are over 20% with the added benefit of requiring no high-temperature steps.[22] As promising as these material are, they possess several shortcomings. All high efficiency HP materials contain lead, which has environmental health risk.[23] HP materials also have limited lifespans owing to low thermodynamic stability of the compound[24], degradation in the presence of light and moisture[25] or light-induced phase segregation.[24] However, these materials have remarkable properties and defect tolerance. The origins of this defect tolerance comes from partial oxidation of Pb^{2+} $6s^2$ electrons.[26] These $6s^2$ electrons give rise to a valence band maximum consisting of anti-bonding orbitals and a conduction band minimum consisting of bonding orbitals. This means that dangling bonds from vacancy formation appear as resonances within the bands, rather than as trap states in the band gap.[27] Bi^{3+} likewise possesses this beneficial electronic structure, and it is expected to possess a similar defect tolerance.[27] BiI_3 is composed of layers of edge-sharing BiI_6 octahedra (where one-third of the Bi sites are vacant) held together in part by van der Waals interacrtions.[28] Lehner et al. have found that BiI_3 has a large static dielectric value with principal components of the static dielectric tensor of $\varepsilon^{\infty}_{xx} = 18.9$ and $\varepsilon^{\infty}_{zz} = 15.0$, which may indicate effective screening of charged point defects, thus improving transport.[29] BiI_3 has also shown lifetimes of over 7 ns at carrier concentrations of 10^{14} cm^{-3}.[26] However, this carrier

concentration corresponds to about 10 Suns. At one Sun, a material with a lifetime of ~10 ns has a steady-state carrier concentration of about 10^{13} cm^{-3}. This is promising since at lower injection levels, the lifetime is likely higher. Materials with lifetimes of at least 1 ns (such as CZTS, InP, and CIGS) have achieved device efficiencies of greater than 10%.[26] Furthermore, materials such as BiI_3 are already well-established as materials for room temperature gamma-ray detectors[30], owing to the high interaction cross section. Bi^{3+} has other advantages over Pb^{2+}, namely that it is less toxic. For instance, bismuth is already in widespread use as the major component of lead-free solders. Compared to lead, mercury, and arsenic, bismuth is the least toxic due to its low water solutbility.[31] While the World Health Organization (WHO) has set a standard of 10 ppb for lead in drinking water,[32].in contrast, no limits have been imposed for bismuth. Finally, BiI_3 has a 1.8 eV band gap and high absorption coefficient.[28] Using the absorption coefficient data presented by Brandt et al.[28], a 500 nm thick film would be sufficient to absorb 95% of incident above-band gap photons. A 1.8 eV band gap BiI_3 top cell would be well-matched with a 1.12 eV Si bottom cell, which would give a maximum theoretical efficiency of 45.3% in a four-terminal tandem configuration.[33]

Processing variables such as substrate temperature during PVD or even choice of solvent for solution processing[28] greatly impact the morphology of the BiI_3 film. Bridgman growth[30] and vacuum based methods[28] are typical and are well developed techniques for making BiI_3 films. Solution processing routes are less well developed. BiI_3 has been solution deposited from DMF[28, 34], THF[34], and DMSO.[35] In fact, bismuth trihalides are known to form coordination compounds with all of these solvents.[35, 36] These solvents are similar in that they possess Lewis base sites, which result in the solvent and BiI_3 forming Lewis acid-base adducts. Solution processed BiI_3 is first spin coated and then solvent vapor annealed to grow larger grains.[34] In solvent vapor annealing

(SVA), films are heated in the presence of solvent vapor (using solvents that have affinity for BiI3). Thus, while DMF, THF, and DMSO may be suitable SVA solvents, the SVA mechanisms are not well known.[37] In general, it is thought that the presence of solvent vapor increases mobility of molecular species in the film and allows the film to re-organize and perhaps achieve larger grains.. DMF SVA has been used previously in the hybrid perovskites to grow grains 1 μm in dimater.[38] However, SVA is sensitive to the environment. Solvent choice and atmosphere[34] as well as humidity[39] are known to change the outcome of the SVA process.

Here, we present an investigation of important variables affecting solvent vapor annealing of BiI_3 films, such as temperature, ambient atmosphere, and water concentration. We used DMF as the SVA solvent as it forms a mildly stable BiI_3-DMF complex[35], which plays a role in growing good morphologies. A coordination compound forms when there is high enough DMF vapor pressure and allows the film to re-organize. However, upon exposure to solvent-free atmosphere, the DMF quickly leaves allowing BiI_3 to re-crystallize. This behavior is in contrast to other BiI_3 complexes. BiI_3-THF solvent complexes are too unstable to use as an effective growth medium, owing to the high vapor pressure of THF, which causes the solvent complex to rapidly degas. BiI_3-DMSO complexes are more stable than the THF or DMF complexes, which leads to poor recrystallization of BiI_3. We show that tuning of water vapor concentration and temperature is crucial to growing large grained, void free, solution processed BiI_3 films, and that the presence of ambient oxygen is less crucial. We present a mechanism for the action of both water and temperature. Through this understanding, we present an optimized SVA process for growing continuous BiI_3 films on TiO_2 substrates.

2.2 Experimental Materials and Methods

Materials. 200 mg/mL BiI_3 inks were prepared by dissolving BiI_3 (99.999%, Alfa Aesar) in anhydrous tetrahydrofuran (THF) (99.9%, inhibitor free, Sigma-Aldrich). inside a N_2 filled glove box. The inks were sealed and then mixed with an ultrasonicator immediately before use. 14x14 mm fluorine-doped tin oxide (FTO) substrates (TEC 7, Sigma-Aldrich) were sequentially cleaned by sonication in a detergent solution, DI water, acetone, and 2-propanol for 10 minutes. Substrates were cleaned with an Ar plasma immediately before use. TiO_2 solutions were prepared by mixing 10 mL ethanol (200 proof, Sigma-Aldrich), 69 µL HCl (37% wt., aq., Macron Fine Chemicals), and 0.727 mL Ti(IV)ethoxide (Aldrich) and sonicating it for 30 minutes. This solution was spin coated onto the FTO substrates in air at 2,000 rpm for 15s. Substrates were coated twice, with a 500 °C air anneal between layers. See Supplemental Information for full details of TiO_2 deposition. BiI_3 inks were deposited on the TiO_2-coated substrates by spin coating at 2,000 rpm for 35s inside a N_2 filled glove box and in a fume hood. After spin coating, the films were solvent vapor annealed (SVA) for 10 minutes with dimethylformamide (DMF)-water mixtures. SVA (Figure S1) consists of three steps: 1) the as spin-coated BiI_3 film is set inside a petri dish on a hotplate; 2) after 60s, solvent is added to the petri dish with the film and the lid is closed; 3) after 9 minutes, the lid is removed so that the film is exposed to the ambient atmosphere for 60s to remove residual DMF and water. DMF concentration was held constant at 10 ppm and water content was varied to achieve 0%, 35%, or 70% relative humidity (RH) at either 80 °C, 100 °C, or 120 °C. See the Supplemental Information for details on the SVA setup and RH calculations. HTLs were prepared by either thermally evaporating ~40 nm V_2O_5 (99.99%, Alfa Aesar) from a tungsten boat at a base pressure of $1x10^{-6}$ Torr or by spin coating spiro-OMeTAD as described elsewhere.[16] The spiro-

OMeTAD was doped with Li and Co and oxidized overnight. Devices were finished by thermal evaporation of ~100 nm Au at a base pressure of $1x10^{-6}$ Torr.

Characterization. Scanning electron microscope (SEM) images were collected at 5 kV accelerating voltage with an FEI XL830 Dual Beam SEM/FIB. Crystallographic measurements were collected with a Bruker D8 Discover XRD. Absolute intensity photoluminescence (AIPL) measurements were collected at 1 Sun photon flux with an apparatus described previously.[40, 41] The 1 Sun condition used corresponds to a photon flux of 1.28×10^{21} photons/s-m^2 at a laser wavelength of 532 nm. A 150 lines/mm Czerny-Turner monochromator blazed at 500 nm was used to collect the signal. Photoluminescence quantum yield (PLQY) and the peak position were used to calculate the quasi-Fermi level splitting (QFLS) and the optoelectronic quality (chi).[41] PV devices were tested in air using a AAA solar simulator (Oriel Sol3A) and a Keithley 2400 SMU. The photoconductivity method was used to determine the mean carrier diffusion length[42, 43] using a bias of +20V with a 432 nm blue LED at 3.66×10^{21} photons/s-m^2 flux, which is 2.8 Suns equivalent for a 1.8 eV band gap material. Photoconductivity measurements were made inside a temperature controlled stage held at 20°C.

2.3 Effect of Water, Temperature, and Solvent on BiI_3 Morphology

Pre-SVA films are dense, but small grained (Figure 3a). SVA grows the grains (Figure 3b and c), but the morphologies are not always the same. We noticed that films prepared in the fume hood with SVA at 100 °C on different days have very different morphologies. These films were prepared under the exact same conditions, with the only difference being the humidities on these days. Indeed, it is known that RH can have a significant influence on SVA.[39] We see disconnected, disc-shaped grains (Figure 3b) whereas films prepared at a different day showed large, uniform, dense

grains (Figure 3c). To better understand this, we treated BiI_3 films with SVA at different temperatures and RH.

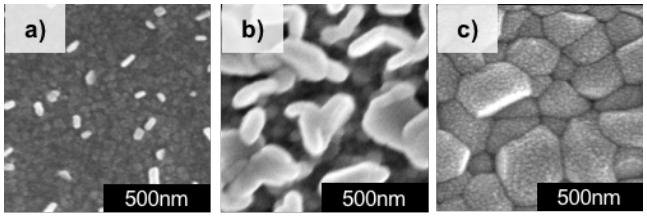

Figure 3. SEM images of BiI_3 films grown on FTO/TiO_2 substrates a) after spin coating and before SVA; post DMF SVA on days with b) lower RH and c) higher RH.

We prepared films treated with SVA at 0%, 35%, and 70% RH at 80 °C, 100 °C, and 120 °C SVA both in a fume hood, but also inside a glove box to investigate the effect of ambient atmosphere. The relevant parameter is actually the activity of the water, which is proportional to the vapor phase mole fraction. The vapor phase mole fraction is related to the water concentration, assuming all the water introduced during the start of SVA goes into the vapor phase. Water concentrations for a RH/T combination are given in Table 1 as g water/cm^3. Multiplying this number by the SVA inner petri dish volume gives the total mass of water needed for SVA. It is this mass of water that was mixed with DMF to create the water-DMF SVA solvent mixtures. We observe that all of the SVA solvent is in the vapor phase by the end of SVA. Some solvent and water loss is expected as the SVA petri dishes are not sealed. SVA is performed inside a smaller petri dish enclosed in a larger petri dish to maintain temperature, reduce airflow effects, and to limit material loss. For convenience, we will continue to refer to RH instead of the total water concentrations. It is important to note that films prepared in ambient air have additional water exposure from ambient RH. On the days we prepared our films in air, relative humidity was 42% at 20 °C, which corresponds to an additional water content of 7.2×10^{-6} g/cm^3 which is less than 7% of the total water concentration and will hence be neglected in the following.

Table 1. Water concentrations (g/cm^3) corresponding to a given T and RH.

	0% RH	35% RH	70% RH
80 °C	**0**	**1.02×10^{-4}**	**2.03×10^{-4}**
100 °C	**0**	**2.06×10^{-4}**	**4.12×10^{-4}**
120 °C	**0**	**3.82×10^{-4}**	**7.64×10^{-4}**

Films prepared from concentrated inks exhibited cracking after spin coating (Figure 4a). Note that the BiI_3 concentration in this study is twice that in previous work.[34] This cracking comes from tensile stresses in the film as the THF rapidly evaporates.[44] We developed a modified ink to prohibit cracking. Addition of 1-2 vol.% DMSO to the THF inks prevented cracking and resulted in smooth films (Figure 4b). Visually, the pure THF and THF+DMSO films are different. The pure THF films are dark after spin coating, owing to the rapid THF evaporation leaving a pure BiI_3 phase behind. The THF+DMSO films are dark red after spin coating. This red color indicates the presence of a BiI_3-DMSO complex in the film.[35] Within 20 minutes exposed to ambient air these films gradually turn black indicating that the BiI_3-DMSO complex is not stable at room temperature, thus decomposes to leave behind the pure BiI3 phase. This slow decomposition process accompanied by the evaporation of DMSO helps in obtaining uniform BiI3 film nucleation and growth, which is a similar behavior observed in hybrid perovskites.[14] We also tested DMF as an additive to the BiI3/THF inks, but this resulted in films that were not dense (Figure S2).

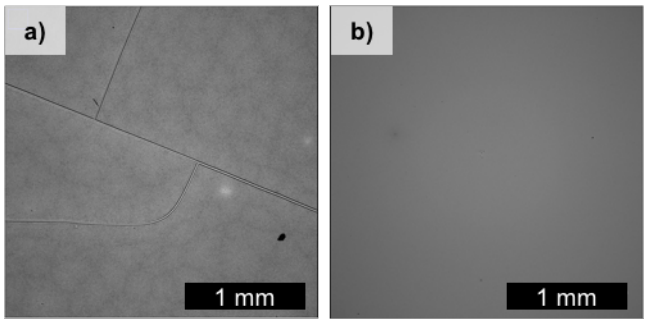

Figure 4. Optical microscope images of BiI_3 spin coated on FTO/TiO_2 films from 200 mg/mL inks containing a) pure THF and b) THF+1 vol. % DMSO.

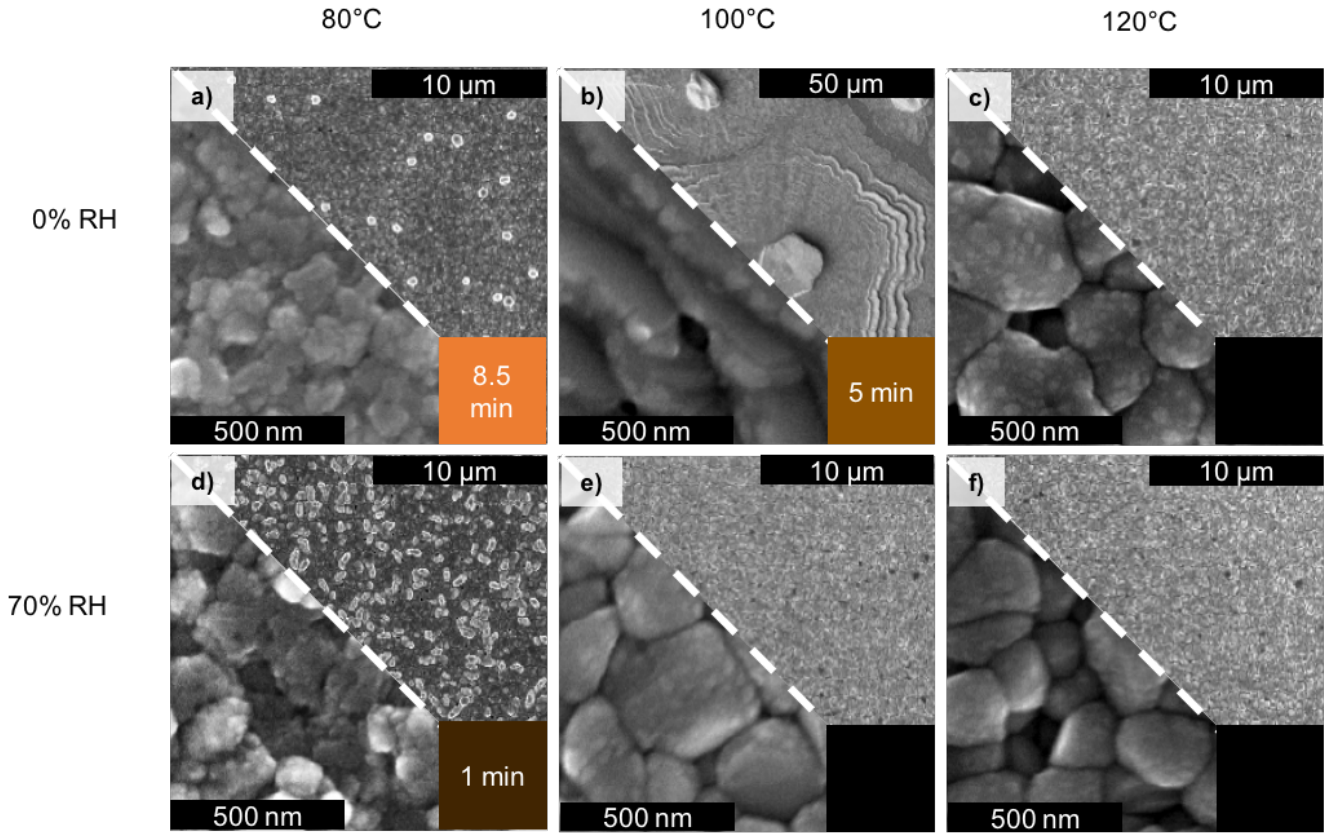

Figure 5. SEM images of BiI_3 films on FTO/TiO_2 prepared in air with the given relative humidity (rows) and temperature (columns) during SVA. The upper and lower halves of each panel are low and high magnification images of the same sample made at the given RH and T. Scale bars are labeled in each image. The colored swatch in the lower right corners of each panel represent the approximate amount of time the sample remained orange during the second step of SVA. Swatches that are primarily orange mean the sample turned orange early on, whereas all black swatches mean the sample never changed color. Times inside the orange swatches are the times that the films remained orange.

SEM images of films after SVA treatment with different RH and temperature are presented in Figure 5. Each of the panels in Figure 5 represent one film, prepared at one SVA condition. This colored swatch in the lower right-hand corner of each panel indicates the color transformation of the films during SVA. A brighter orange swatch means the film turned orange early on during the second step of SVA. The darker the swatch, the longer the film took to turn orange. All black swatches mean the films never changed color. The times listed in the orange swatches are the times the films were orange. The films prepared at 80 °C and 0% RH (Figure 5a) remained orange until it was uncovered. This indicates that even though the petri dishes are not sealed, they retain SVA solvent for the duration of SVA.

All films prepared with SVA at 80 °C turned orange during step two (solvent addition) of the SVA process, independent of RH. However, the time it took the films to turn orange increases with RH. The film prepared at 80 °C and 0% RH (Figure 5a), turned completely orange within 30 s of solvent addition. For the same temperature, films prepared at 35% (Figure S3) and 70% RH (Figure 5d) turned completely orange 7 min and 9 min into SVA respectively. The film prepared at 100 °C and 0% RH showed a non-uniform behavior: part of the film turned orange 60 s into SVA and part remained black (Figure 6a). SEM of the orange part of this film is shown in Fig. 5b. This is in good agreement to our initial findings where we observed morphological differences with films treated with 100 °C SVA under different ambient humidities. The partial color change indicates that the portion of the substrate that turned orange experienced a higher DMF partial pressure than the portion that stayed black. The region that turned orange was the side of the substrate closest to the DMF source. During the final step of SVA, where the lid is opened so that the solvent could escape, all orange films immediately turned black again. No color change was observed for the 100 °C+35% RH (Figure S3), 100 °C+70% RH (Figure 5e), or any of the films made at 120 °C

(Figure 3c and f). Visually there is a difference between films that turned orange during SVA and those that stayed black: films that turned orange are hazy whereas those that did not change color remain relatively shiny. The haziness of the films that turned orange during SVA comes from the larger domains (1-20 μm) that developed in the film (Figures 6b). The larger domains result in films with higher surface roughness, which is what produces the scattering. From here on, we will refer to the films that turned orange during the second step of SVA as "orange films" and the films that did not change color during SVA as "black films" for convenience.

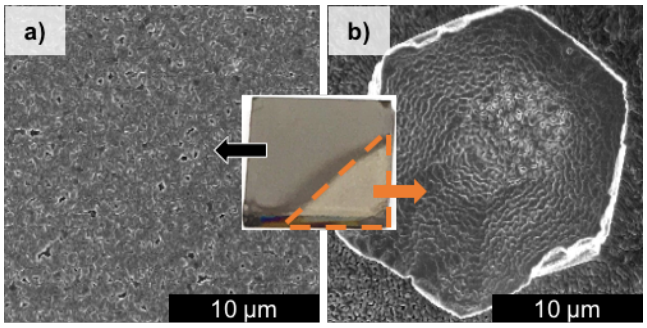

Figure 6. SEM images of the BiI_3 film prepared with SVA at 100°C and 0% RH. a) Region of the film that turned black and b) region of the film that remained orange.

The orange films at 80 °C (Figure 5a and d) have larger domains sitting on top of the films. The larger domains scatter light more than the films with smaller domains, and thus these films appear more hazy. Looking at the higher magnification images, we see that the film is primarily made of clusters of small (<100 nm dia.) grains. The film that experienced the plume of DMF (Figure 5b) now consists of large platelets (~15 μm dia.). The differences between this case and the 80 °C cases are attributable to the high DMF concentration in the plume. All of the black films are similar (Figure 5c, e, and f), consisting of apparent grain sizes of 300-500 nm diameter as determined by SEM. This means that as long as the films do not change color during SVA, dense, large-grained films can be grown.

Films made inside and outside of a glove box with the same SVA condition have similar morphologies. For instance, films made with SVA at 120 °C and 70% RH inside (Figure 7a) and outside (Figure 7b) a glove box show similar SEM grain size (300-500 nm) and polydispersity. This shows that ambient environment does not have a big impact on morphology. We will focus on films prepared outside a glove box for the rest of our discussion. Full comparison of glove box and air films is given in the supplement (Figure S3 and S4).

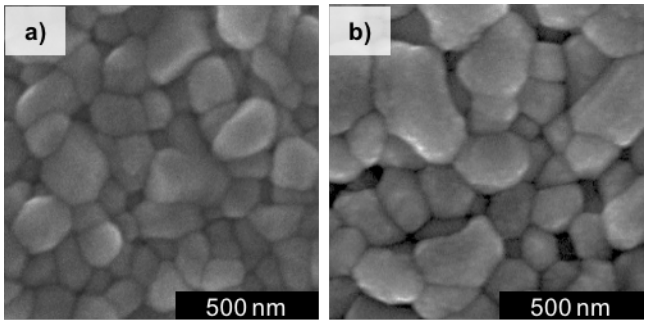

Figure 7. SEM images of BiI_3films on FTO/TiO_2 substrates grown with SVA at 120°C and 70% RH a) inside and b) outside a glove box.

2.4 Mechanism of Water, Temperature, and Solvent on BiI_3 Morphology

We explain the role of SVA temperature and water concentration by considering the BiI_3-DMF complexation chemistry. Norby et al.[35] have determined via single-crystal XRD that the carbonyl oxygen in DMF complexes with the Bi^{3+} center to give a solvent complex crystal with a unit cell of $Bi(DMF)_8$-Bi_3I_{12}. Octahedral complexes such as BiI_3 typically undergo ligand exchange via a dissociative interchange mechanism (I_d).[45] In an I_d mechanism, the bond with the incoming group is formed at the same time the bond with the leaving group is broken. In our case, the incoming group is the carbonyl group on the DMF and the leaving group is an iodide anion. Bi^{3+} is a Lewis acid of intermediate hardness. The oxygen in the DMF carbonyl group is a hard base, and the iodide anion is a soft base.[46] As a result, Bi^{3+} is expected to have a similar ability to complex with

the carbonyl oxygen in DMF and the iodide. Furthermore, as has been shown by Sanderson et al., the bond dissociation enthalpy of the Bi-I bond is the smallest for the Bi-halides (i.e. the Bi-I bond is easier to break than other Bi-halide bonds).[47] The character of the bond is largely ionic, and the large ionic radius of the iodide anion means it is held less strongly by the Bi^{3+} center due to electron-electron repulsion between the Bi and I. The ionic character of the Bi-I bond is critical for facile DMF complexation. The I_d mechanism requires a good leaving group. Because the Bi-I bond is more ionic than covalent and thus more easily broken, the iodide makes a good leaving group, allowing the DMF to readily complex with the Bi^{3+} center.

We first consider the water-free (DMF vapor only) 80 °C case. The spin-coated crystalline BiI_3 film is made up of BiI_6 octahedra arranged in 2-D sheets.[28] Consider a single BiI_6 octahedron exposed to DMF vapor. The DMF approaches the Bi^{3+} center and begins to form a Bi--OR complex with the DMF carbonyl oxygen. At the same time, the Bi-I bond is being broken and the I^- leaves. This reaction continues to take place until the Bi center is coordinated to eight DMF molecules $[Bi(DMF)_8]^{3+}$, which is charge balanced by a $[Bi_3I_{12}]^{3-}$ group. If enough DMF is present, the entire film is transformed to a DMF-BiI_3 coordination compound. This compound may crystallize with a unit cell composed of four $Bi(DMF)_8$-Bi_3I_{12} pairs, as shown by Norby et al.[35] We note that a similar hybrid structure also forms with DMSO (Figure S5). The DMSO coordination compound[35] has stoichiometry $Bi(DMSO)_8 \cdot Bi_2I_9$. Because our inks contain DMSO, the films contain some amount of this BiI_3-DMSO solvent complex immediately after spin coating. As mentioned, the presence of the DMSO helps prevent cracking. The slow decomposition of the BiI_3-DMSO complex into crystalline BiI_3 is what prevents cracking. THF will also form coordination compounds with BiI_3 as evidenced by the high solubility of BiI_3 in THF. In solution, the THF is able to complex with BiI_3 via the Lewis basicity of the THF oxygen. However, the BiI_3-THF

complex breaks apart quickly due to the high vapor pressure and rapid evaporation of THF. As soon as the solution is spin coated, the THF rapidly leaves, leaving behind crystalline BiI_3. This is why the longer-lived BiI_3-DMF and BiI_3-DMSO solvent complexes are the relevant species for understanding the evolution of BiI_3 morphology during SVA.

The BiI_3-DMSO coordination compound that is the orange phase witnessed under low RH and low T.[35] The solvent complex film is thicker than the BiI_3 film due to DMF uptake. The lattice constants of hexagonal BiI_3 are a = 7.519 Å and c = 20.721 Å[30], and the lattice constants of the BiI_3-DMF complex crystal are a = 15.116 Å, b = 30.875 Å, and c = 15.744 Å.[35] These correspond to unit cell volumes of 1.17 nm^3 and 7.35 nm^3 for the BiI_3 and the BiI_3-DMF crystal respectively. This means that a BiI_3 film on a 14x14 mm substrate that was originally 200 nm thick becomes more that 1200 nm thick. Upon drying, this film collapses back to the BiI_3 film, which results in a different morphology relative to the initial (pre SVA) BiI_3 film. This can lead to very rough films with large BiI_3 clusters as shown in Fig. 5a) and d) or to films with large, disconnected platelets as shown in Fig. 6b. If a BiI_3 film is exposed to DMF vapor for a much longer time than the 9 minutes in our SVA process then macroscopic morphologies can form as shown in Fig. S6.

The morphology of the initially crystalline BiI_3 film is significantly affected by the complexation with DMF and leads to a partially amorphous phase. Upon DMF evaporation, crystalline domains regrow starting from nucleation centers. The mechanism of grain growth during SVA is not well-understood.[37] However, it is thought that the presence of a solvent (in which the film material is soluble) creates a more fluid environment in which the component species can diffuse greater distances.[38] In the case of the BiI_3-DMF system, the formation of the solvent complex could be the origin of the enhanced diffusion.

Now consider the case of SVA at higher temperatures (T ~120 °C). We did not observe the orange phase forming during SVA at this temperature with the DMF concentrations considered. To better understand this, we collected data to perform a Van 't Hoff analysis (details in the Supplemental Information). The reaction considered is $4\ BiI_3 + 8\ DMF \leftrightarrow [Bi(DMF)_8]^{3+}[Bi_3I_{12}]^{3-}$. BiI_3 films were placed in sealed vials with different DMF and water dosings. The BiI_3 films were allowed to complex with the DMF at room temperature until the orange solvent complex formed. The vials were then heated in a box oven, slowly increasing temperature until the films turned black again. From this, we get the equilibrium constant for the BiI_3-DMF complexation. By plotting $\ln(K_{eq})$ vs. 1/T, we can extract ΔH_{rxn} and ΔS_{rxn} for the system. On the basis of the stoichiometry of the above reaction, this yielded values of ΔH_{rxn} of -3 ± 1 eV and ΔS_{rxn} of -0.006 ± 0.003eV/K per molecular of the coordination compound. If one assumes that each successive DMF addition has similar thermodynamics, the enthalpy and entropy are ΔH_{rxn} of -0.4 eV and ΔS_{rxn} of -0.0007 eV/K per DMF. This means that this reaction is enthalpically favorable up to 227 °C, at which point the entropic term begins to dominate. At temperatures exceeding 227 °C, no concentration of DMF would result in the films turning orange. At elevated temperatures, it is more favorable for the DMF to be in the vapor phase, rather than to be complexed with BiI_3. It is this effect that prevents the orange solvent complex from forming at higher SVA temperatures, independent of RH.

Now we discuss the effect of water on the SVA process. At 80°C, RH slows down the transformation of the BiI_3 into the orange film. At 100°C, the presence of water prevents the film from turning orange at all and results in more uniform grain growth. To understand this, we note that hydrogens in water will hydrogen bond with the oxygen in DMF. As a result, the electron donating strength (i.e. the Lewis basicity) of the carbonyl oxygen is reduced. Thus, the DMF is rendered less reactive and will complex less readily with the BiI_3. This would be expected for cases

where the water concentration is equal to or greater than the DMF concentration, which is true at the DMF:water dosings used during SVA. This explains the difference we see between films prepared at 100°C with 0% and 70% RH.

2.5 Effect of Substrate on BiI_3 Morphology

We spin coated 200 mg/mL BiI_3 in THF + 1-2 vol.% DMSO onto FTO/TiO_2, FTO/ZnO, ITO/Cu:NiO_x substrates. We observe significantly different film morphologies with the different substrates. Films grown on TiO_2 (Figure 8a) are made of 300-500 nm, densely packed grains. Films grown on ZnO (Figure 8b) are more polydisperse and contain small and large platelets with sharp edges. Films prepared on copper-doped nickel oxide (Cu:NiO_x) (Figure 8c) are also more polydisperse than the films grown on TiO_2, but also contain large (1 µm dia.) platelets. We rationalize these observations by noting that film-substrate surface energy differences can also influence film growth. In cases where substrate surface energy is smaller than film + interface surface energies, island growth is expected.[48] Other factors like deposition temperature also can impact crystal growth.[28] This means that by optimizing parameters like SVA solvent, water concentration, and temperature, we might be able to obtain dense films with the desired grain size for each choice of substrate.

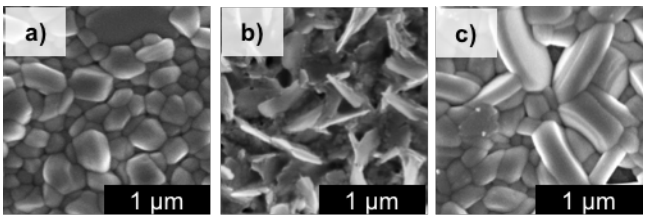

Figure 8. SEM images of BiI_3 films grown with SVA at 120°C and 70% RH on a) FTO/TiO_2, b) FTO/ZnO, and c) ITO/Cu:NiO_x.

2.6 Effect of Water, Temperature, and Solvent on BiI_3 Crystallographic Orientation

XRD spectra for BiI_3 films grown at different SVA temperatures and water vapor concentrations are shown in Figure 9. The orange films, i.e. those grown at 80 °C (0% RH and 70% RH) and 100 °C (0% RH) show a significantly different pattern than the black ones. The most pronounced XRD peaks for the orange films are due to reflections at (003), (006), (009), and (00 12) planes which belong to the same family of (00l) planes. This indicates a texturing of those films. In contrast, the black films show much smaller peaks for the (00l) planes. We observe pronounced reflections at (113) and (300) in the black films, indicating less texturing.

To further study this texturing effect, we evaluate the texture coefficient (TC). TC of a plane (hkl) is defined as $TC(hkl) = \frac{I(hkl)/I_0(hkl)}{[\sum I(hkl)/I_0(hkl)]/N}$, where I(hkl) is the measured intensity, I_0(hkl) the intensity of the powder diffraction, and N is the number of planes considered.[49] A TC equal to 1 indicates no preferred orientation. The TC for (300), (113), and (003) planes are shown in Figure 10 for different SVA temperatures and water concentrations. All films that turned orange during SVA, i.e. at 80 °C show a TC of around 3 for the (003) plane and of close to 0 for the (113) and (300) planes. We note that the same TC's are also observed for the orange films at 100 °C, 0% RH. This indicates a strong texturing: The orange films are oriented with their (003) plane predominantly parallel to the substrate, i.e. the BiI_3 film is layered in such a way that the planes which contain edge shared BiI_6 octahedra are parallel to the substrate. The black films do not show this texturing: TC for the (003) and (113) planes is between 0.5 and 0.9 whereas the TC for the (300) plane is around 1.5. This indicates a slightly preferred oriented in such a way that the edge shared BiI_6 planes are perpendicular to the substrate. Similar texturing has been found in BiI_3 films that have formed from BiI_3-DMSO complexes.[35]

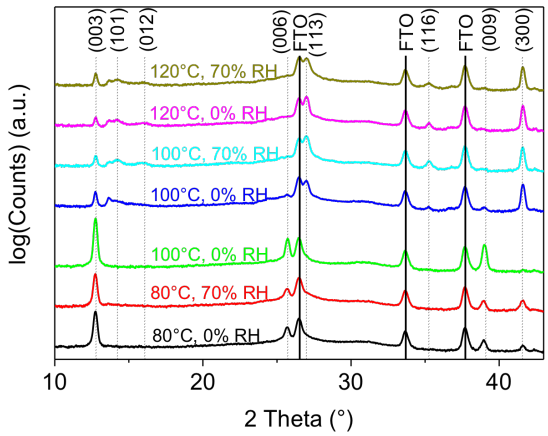

Figure 9. XRD spectra as a function of SVA temperature and relative humidity. Green and blue curves show spectra for those areas which turned orange and which stayed black, respectively (see Fig. 4). Dotted vertical lines indicate BiI_3 powder peaks. Solid black vertical lines indicate the peaks of the FTO substrate.

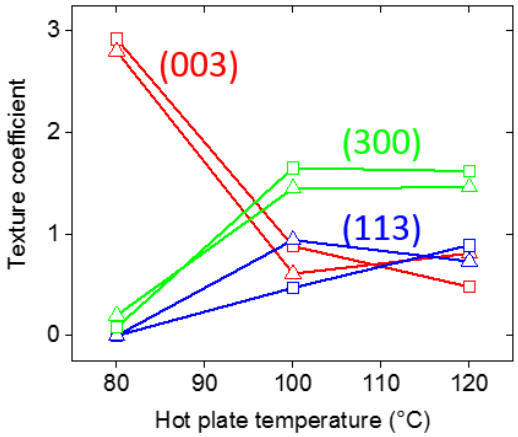

Figure 10. Texture coefficients related to the (300) plane (green), (113) plane (blue), and (003) plane (red) as a function of SVA temperature for 0% RH (open squares) and 70% RH (open pyramids).

2.7 Effect of Water, Temperature, and Solvent on BiI_3 Optoelectronic Quality

We performed absolute intensity photoluminescence (AIPL) measurements at a photovoltaic device relevant excitation laser intensity comparable to one Sun (100 mW/cm^2). Photoluminescence measurements on BiI_3 films have been carried out previously[28, 34], however, since the PL quantum yield (PLQY) is very low, those measurements used laser excitation intensities comparable to > 100 Suns. Here, we were able for the first time to measure BiI_3 AIPL at 1 Sun effective intensities. This was enabled both by the high quality of the films and a modification to our measurement technique (see SI for details).

The AIPL is peaked at 1.78 eV with a full-width half max of 184 meV (Figure 11a, blue trace). This is very close to the measured band gap of 1.79 eV determined from UV-Vis absorption measurements (Figure 11a, red trace). The fact that the PL peak is right at the band edge indicates that sub-band-gap states should not cause a significant loss of voltage. From AIPL, we get the photoluminescence quantum yield (PLQY), which we used to calculate the quasi-Fermi level splitting (QFLS) (Figure 9b) with the method described in Braly et al.[41] The QFLS is an indication of the maximum voltage V_{oc} achievable by a solar cell device. QFLS is proportional to $kT \ln(1/PLQY)$. Therefore what may appear as larger differences in PLQY do not correspond to as large differences in QFLS. In Figure 11b, we also show the ratio of the measured QFLS to the Shockley-Queisser QFLS ($QFLS_{SQ}$) for a material with the same bandgap, $\chi = QFLS/QFLS_{SQ}$.[41] Chi may be considered the optoelectronic quality of the material. All films prepared at 80 °C as well as the film prepared at 100 °C with 0% RH have PLQY < 1×10^{-5} %. The films prepared at 100 °C with 35% and 70% RH and all the 120°C films have PLQY values of 2×10^{-5} %. Full AIPL data for all T, RH, and environment are given as Figures S7 and S8.

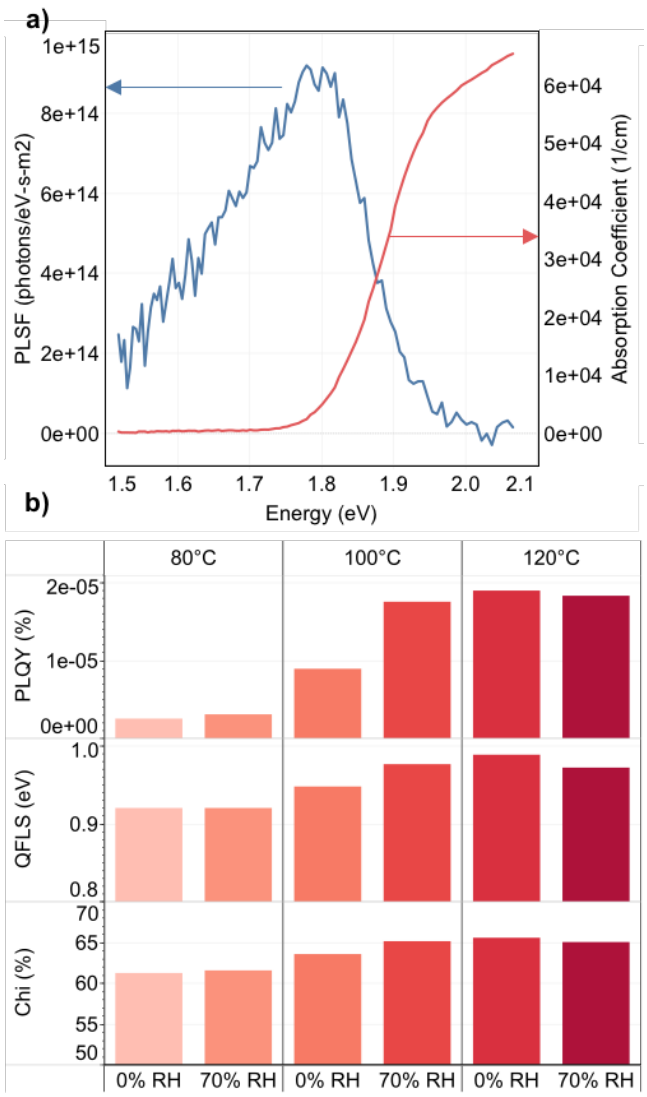

Figure 11. a) AIPL spectrum of BiI_3 with peak at 1.78 eV. b) PLQY, QFLS, and Chi from one sun AIPL of BiI_3 films prepared with different SVA conditions.

The lower PLQY films were the orange films (i.e. the films that turned orange during the second step of SVA), whereas the higher PLQY values were obtained from the black films. PLQY was greater by 2-6x in the black films over the orange films. This may be understood as an effect of the grain size. The films that turned orange during SVA have grains with diameters ≤ 100 nm. The films that remained black have grains 300-500 nm in size. The differences in PLQY may be attributed to non-radiative recombination at the grain boundaries or within the bulk. The smaller

grained films have a greater number of grain boundaries, meaning non-radiative recombination would be greater. However, we cannot exclude differences in the bulk. Films that turned orange during SVA may have entrained DMF within the crystalline BiI_3. This may give rise to different point defects and contribute to non-radiative recombination.

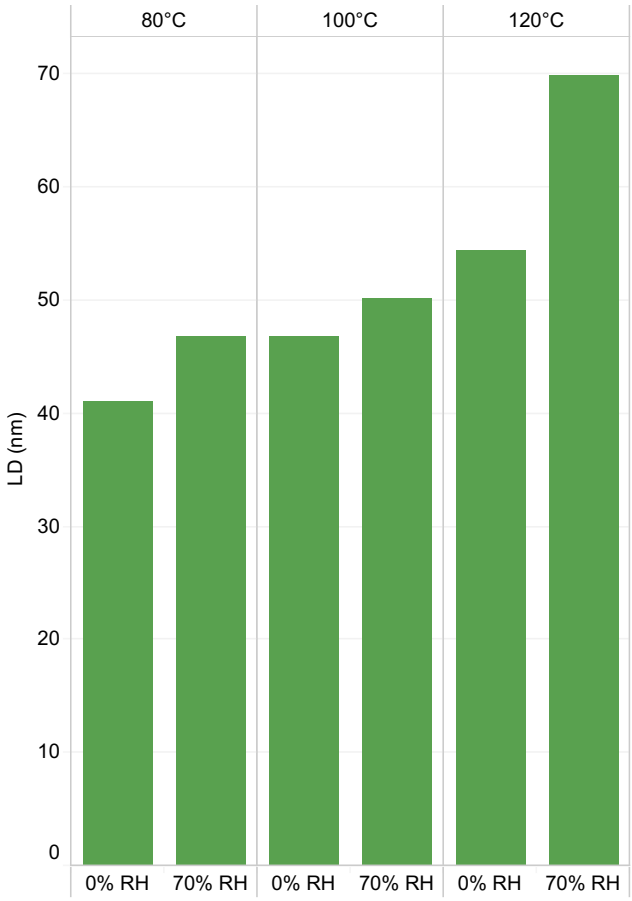

Figure 12. Two-point lateral DC photoconductive diffusion length measurements of BiI_3 films grown with different SVA temperatures and RH.

A lateral DC photoconductivity method[42,43] was used to estimate the effective diffusion length (Figure 12) to assess the impact of SVA on carrier transport. The diffusion length (L_D) determined from this technique is an average of the electron and hole diffusion lengths. The orange films were found to have $L_D < 45$ nm, whereas all the black films have $L_D > 50$ nm. The film prepared at 120°C and 70% RH has $L_D \sim 70$ nm, which is 1.7 times greater than the film prepared at 80°C and

0% RH. The differences in L_D likely arise from the smaller grains. This shows that tuning SVA to grow large grained, dense films not only yields higher QFLS but also better transport, which is crucial for making good PV devices.

2.8 BiI_3 Photovoltaic Devices

We made PV devices to assess the impact of SVA on PV performance. We report current-density versus voltage (JV) curves and time-dependent power conversion efficiency (using maximum power-point tracking[50]) under continuous simulated AM1.5G illumination. Our best cells were made with spiro-OMeTAD as the hole transporting layer, rather than V_2O_5. The best spiro-OMeTAD cell processed inside a glove box with the optimized SVA process (120 °C+70% RH) has a stabilized PCE (Figure 13b, blue curve) of 0.51%. An orange film device (80 °C+70% RH) in the same architecture shows a much lower stabilized PCE of 0.04% (Figure 13c, orange curve). Considering the device made at 120 °C and 70% RH SVA (Figure 13d), the JV curve measured under illumination (blue) is different in shape than the JV curve measured in the dark (orange). The differences we see between the light and dark curves at voltages less than V_{OC} are a consequence of a voltage dependent photocurrent and the light conductivity of the material. The low diffusion lengths measured (70 nm) mean that we are unable to efficiently collect carriers generated more than 70 nm from their respective selective contacts. This is why the short circuit current (J_{sc}) is only 4.14 mA/cm^2. As negative bias increases, we have increasing current as the electric field is now helping to drive carrier collection via an increasing drift component. As we cross into forward bias, the electric field is now causing carriers to drift towards their non-selective contacts, which drives the current down. This voltage dependent photocurrent also explains the low VOC. The voltage dependent photocurrent continues to decrease under forward bias until there is no current flow in the device, yielding small values for VOC. The low diffusion lengths also

imply greater losses dues to recombination, which will also reduce V_{OC}. It is also possible that the differences in shape are a consequence of photo-active shunts. The increased conductivity of TiO_2[51] or spiro-OMeTAD[52] under illumination may result in shunting pathways only becoming active when the device is illuminated. To explain the behavior above V_{OC}, we fit the JV curves. Table 2 shows the results of fitting the non-ideal diode equation (Figure S9) to the light and dark curves for the device made at 120 °C and 70% RH. The reverse saturation currents (J_0) of the light and dark curves differ by an order of magnitude. This implies voltage/illumination dependent changes in recombination. However, the extracted diode quality factor (β) also changes, so attributing changes in the $V>V_{OC}$ region exclusively to changes in the reverse saturation current is not possible.

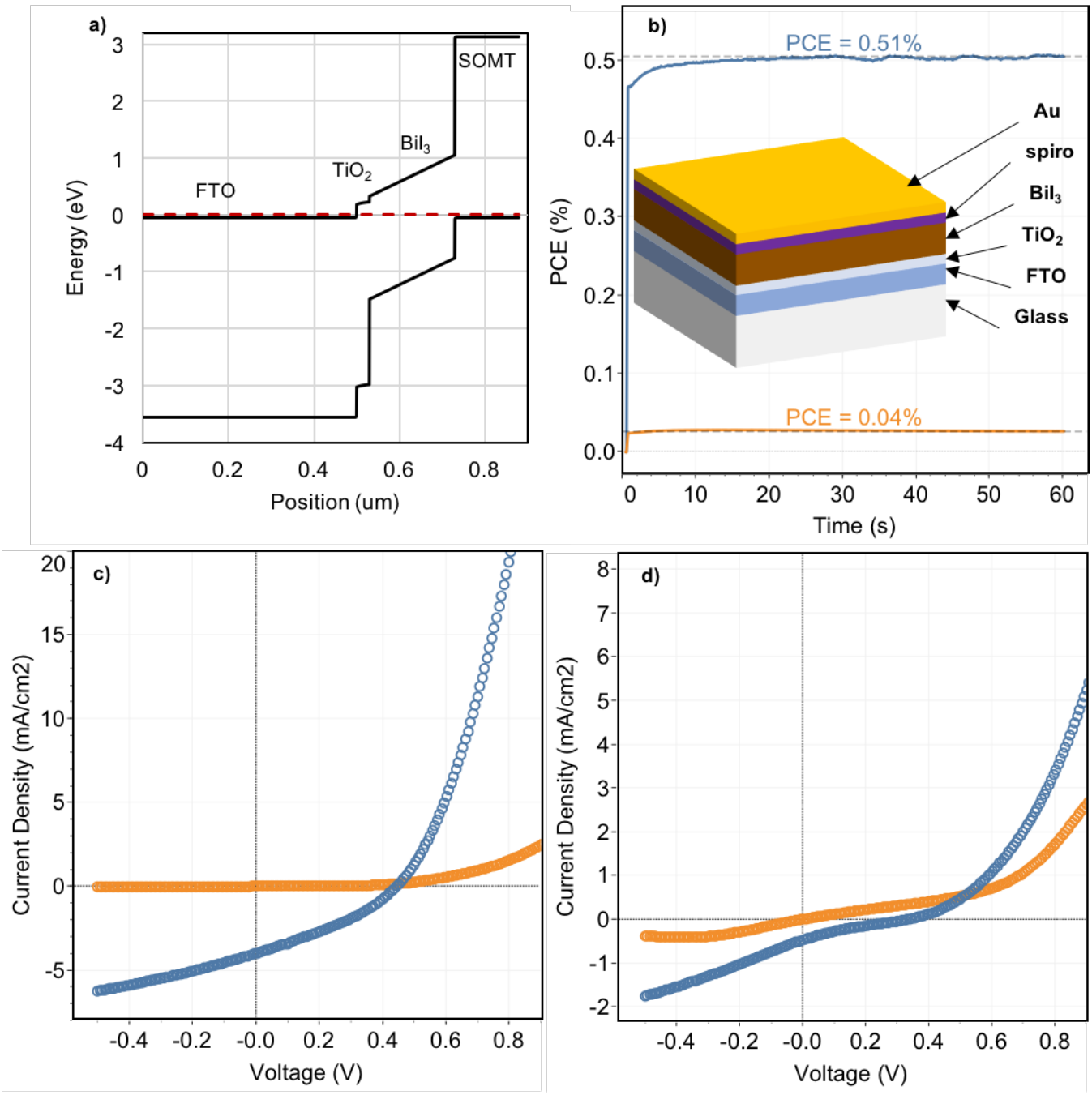

Figure 13. a) Equilibrium band diagram of FTO/TiO_2/BiI_3/spiro-OMeTAD. b) Maximum power point tracking curves for devices made with 120 °C and 70% RH (blue) and 80 °C and 70% RH (orange curve). Inset shows device stack. c) Light (blue) and dark (orange) JV curves for the 120 °C and 70% RH device. d) Light (blue) and dark (orange) JV curves for the 80 °C and 0% RH device.

Let us consider band offsets. The BiI_3 conduction band (CB) lies 4.1 eV below vacuum, and the TiO_2 CB lies 4.2 eV below vacuum.[29] As the difference is only 0.1 eV, we would not expect to have issues extracting photoexcited electrons. Now, if we consider the hole-extracting contact, the band edge of the spiro-OMeTAD lies 5.1 eV below vacuum.[53] Compare this to the position of the BiI_3 valence band, which is 6.1 eV below vacuum.[29] With the given band offsets, we would expect electron and hole extraction driving forces to exist, so this is not a contributing factor to the low V_{OC}. The voltage may instead be limited by the position of the Fermi level in the FTO. Because the FTO is so highly doped, it effectively sets the Fermi level on that side of the device, potentially limiting device voltage. The device made at 80 °C and 70% RH (Figure 13d) similar behavior to the previous device. However, what is different is the presence of an s-shape in the curves. The electronic structure of the BiI_3 that changed color during SVA may be different than a film that stayed black, allowing for the formation of barriers at the interfaces.

Table 2. Non-ideal diode equation fitting results of the device made at 120 °C and 70% RH

	Illuminated	**Dark**
PCE (%)	**0.51**	**-**
V_{OC} (V)	**0.39**	**-**
J_{SC} (mA/cm^2)	**4.14**	**-**
J_0 (mA/cm^2)	**2.48×10^{-2}**	**3.07×10^{-3}**
R_s (Ω)	**166**	**2010**
R_{sh} (Ω)	**5860**	**9.44×10^{5}**
β	**3.46**	**4.33**

2.9 Conclusion

We have demonstrated the roles that temperature and water play in the solvent annealing process for BiI_3 films and developed a reliable process for growing large-grained, continuous films. Films with small grains and poor morphologies result in reduced device performance and optoelectronic quality. Performing SVA with precise dosing of water and DMF grows uniform films with a SEM-based morphological grain size of 300-500 nm. Water acts to moderate the influence of DMF during the SVA process, allowing more controlled growth to occur. Higher temperatures also moderate the action of DMF. Formation of orange BiI_3-DMSO complex during SVA results in films with a preferred orientation. In this case, the predominant BiI_3 plane is the (003) plane. This

is the plane corresponding to the 2D sheets of BiI_6 octahedra. In this case, these sheets are oriented parallel to device contacts. Because the 2D sheets are not connected by ionic (or covalent) bonds, one may guess that carrier transport perpendicular to the sheets may be less efficient between sheets than it is within sheets. However, this is not the case here as these films also have a large number of voids, which reduces L_D more than any orientation effects can compensate for. Carriers are not collected as efficiently, reducing device performance. L_D measurements also show that tuning SVA to give large-grained, continuous films results in larger diffusion lengths. Modifying the ink chemistry with DMSO avoids film cracking.

The 1 eV QFLS is very promising. However, 1 eV is only 65% of the max theoretical V_{oc}, which indicates that there is still room for improvements via defect passivation. QFLS of larger grained films is 100 meV greater than the QFLS of smaller grained films. The differences can be attributed to greater non-radiative recombination in the smaller grained films. The greater non-radiative recombination may be an effect of the larger number of grain boundaries or different point defects in the bulk. The large voltage deficit seen in devices is a consequence low diffusion length and the setting of the Fermi level by the FTO. These low diffusion lengths give rise to a voltage-dependent photocurrent, which is driven to zero at small forward biases. This points to improving diffusion length and device architecture as ways to improve BiI_3 devices.

This work expands the understanding of BiI_3 films and devices, opening the door for improving device efficiencies. Further development of this material could enable it to become a true competitor to PbI_2-based hybrid perovskites, while avoiding the toxicity and stability issues of the perovskite material.

References:

1. World Population Clock. http://www.worldometers.info/world-population/ - table-forecast (14 August),
2. International Energy Outlook 2016. https://www.eia.gov/outlooks/ieo/world.php (14 August),
3. The Consequences of Climate Change. https://climate.nasa.gov/effects/ (14 August),
4. Nozik, A. J., Exciton Multiplication and Relaxation Dynamics in Quantum Dots: Applications to Ultrahigh-Efficiency Solar Photon Conversion. *Inorganic Chemistry* **2005,** 44, (20), 6893-6899.
5. Nelson, J., *The Physics of Solar Cells*. Imperial College Press: London, 2003.
6. Solanki, C. S.; Beaucarne, G., Advanced Solar Cell Concepts. *Energy for Sustainable Development* **2007,** 11, (3), 17-23.
7. De Vos, A., Detailed balance limit of the efficiency of tandem solar cells. *Journal of Physics D: Applied Physics* **1980,** 13, (5), 839.
8. Xin, H.; Katahara, J. K.; Braly, I. L.; Hillhouse, H. W., 8% Efficient Cu2ZnSn(S,Se)4 Solar Cells from Redox Equilibrated Simple Precursors in DMSO. *Advanced Energy Materials* **2014**, 1301823.
9. Collord, A. D.; Katahara, J. K.; Bucherl, C. N.; Hao, X.; Pruzan, D. S.; Hillhouse, H. W., Kesterite Solar Cells: State-of-the-art, Perspective, and Grand Challenges for Copper Zinc Tin Sulfide (CZTS) and Selenide (CZTSe) Materials and Devices. In Unpublished: 2012.
10. Guo, Q.; Ford, G. M.; Yang, W.-C.; Walker, B. C.; Stach, E. A.; Hillhouse, H. W.; Agrawal, R., Fabrication of 7.2% Efficient CZTSSe Solar Cells Using CZTS Nanocrystals. *Journal of the American Chemical Society* **2010,** 132, (49), 17384-17386.
11. Uhl, A. R.; Fella, C.; Chirila, A.; Kaelin, M. R.; Karvonen, L.; Weidenkaff, A.; Borca, C. N.; Grolimund, D.; Romanyuk, Y. E.; Tiwari, A. N., Non-vacuum deposition of Cu(In,Ga)Se2 absorber layers from binder free, alcohol solutions. *Progress in Photovoltaics* **2012,** 20, (5), 526-533.
12. Romanyuk, Y. E.; Hagendorfer, H.; Stucheli, P.; Fuchs, P.; Uhl, A. R.; Sutter-Fella, C. M.; Werner, M.; Haass, S.; Stuckelberger, J.; Broussillou, C.; Grand, P. P.; Bermudez, V.; Tiwari, A. N., All Solution-Processed Chalcogenide Solar Cells - from Single Functional Layers Towards a 13.8% Efficient CIGS Device. *Advanced Functional Materials* **2015,** 25, (1), 12-27.
13. Uhl, A. R.; Katahara, J. K.; Hillhouse, H. W., Molecular-ink route to 13.0% efficient low-bandgap CuIn(S, Se)(2) and 14.7% efficient Cu(In, Ga)(S, Se)(2) solar cells. *Energy & Environmental Science* **2016,** 9, (1), 130-134.
14. Jeon, N. J.; Noh, J. H.; Kim, Y. C.; Yang, W. S.; Ryu, S.; Seok, S. I., Solvent engineering for high-performance inorganic–organic hybrid perovskite solar cells. *Nat Mater* **2014,** 13, (9), 897-903.
15. Lee, M. M.; Teuscher, J.; Miyasaka, T.; Murakami, T. N.; Snaith, H. J., Efficient Hybrid Solar Cells Based on Meso-Superstructured Organometal Halide Perovskites. *Science* **2012,** 338, (6107), 643-647.
16. Saliba, M.; Matsui, T.; Seo, J. Y.; Domanski, K.; Correa-Baena, J. P.; Nazeeruddin, M. K.; Zakeeruddin, S. M.; Tress, W.; Abate, A.; Hagfeldt, A.; Gratzel, M., Cesium-containing triple cation perovskite solar cells: improved stability, reproducibility and high efficiency. *Energy & Environmental Science* **2016,** 9, (6), 1989-1997.

17. Graetzel, M.; Janssen, R. A. J.; Mitzi, D. B.; Sargent, E. H., Materials interface engineering for solution-processed photovoltaics. *Nature* **2012,** 488, (7411), 304-312.
18. Powell, D. M.; Fu, R.; Horowitz, K.; Basore, P. A.; Woodhouse, M.; Buonassisi, T., The capital intensity of photovoltaics manufacturing: barrier to scale and opportunity for innovation. *Energy & Environmental Science* **2015,** 8, (12), 3395-3408.
19. Repins, I. L.; Moutinho, H.; Choi, S. G.; Kanevce, A.; Kuciauskas, D.; Dippo, P.; Beall, C. L.; Carapella, J.; DeHart, C.; Huang, B.; Wei, S. H., Indications of short minority-carrier lifetime in kesterite solar cells. *Journal of Applied Physics* **2013,** 114, (8).
20. Yang, S.; Lin, K. M.; Lee, W. C.; Lo, W. S.; Chen, C. H.; Wu, J. L.; Chiang, C. Y.; Wu, C. H.; Sun, Y. L.; Lo, H.; Chang, C. H.; Chu, L. In *Achievement of 16.5% total area efficiency on 1.09m2 CIGS modules in TSMC solar production line*, 2015 IEEE 42nd Photovoltaic Specialist Conference (PVSC), 14-19 June 2015, 2015; 2015; pp 1-3.
21. Fthenakis, V., Sustainability of photovoltaics: The case for thin-film solar cells. *Renewable & Sustainable Energy Reviews* **2009,** 13, (9), 2746-2750.
22. Shin, S. S.; Yeom, E. J.; Yang, W. S.; Hur, S.; Kim, M. G.; Im, J.; Seo, J.; Noh, J. H.; Il Seok, S., Colloidally prepared La-doped BaSnO3 electrodes for efficient, photostable perovskite solar cells. *Science* **2017,** 356, (6334), 167-171.
23. Green, M. A.; Ho-Baillie, A.; Snaith, H. J., The emergence of perovskite solar cells. *Nat Photon* **2014,** 8, (7), 506-514.
24. Bischak, C. G.; Hetherington, C. L.; Wu, H.; Aloni, S.; Ogletree, D. F.; Limmer, D. T.; Ginsberg, N. S., Origin of Reversible Photoinduced Phase Separation in Hybrid Perovskites. *Nano Letters* **2017,** 17, (2), 1028-1033.
25. Yang, J.; Siempelkamp, B. D.; Liu, D.; Kelly, T. L., Investigation of CH3NH3PbI3 Degradation Rates and Mechanisms in Controlled Humidity Environments Using in Situ Techniques. *Acs Nano* **2015,** 9, (2), 1955-1963.
26. Brandt, R. E.; Poindexter, J. R.; Gorai, P.; Kurchin, R. C.; Hoye, R. L. Z.; Nienhaus, L.; Wilson, M. W. B.; Polizzotti, J. A.; Sereika, R.; Žaltauskas, R., Searching for "defect-tolerant" photovoltaic materials: Combined theoretical and experimental screening. *Chemistry of Materials* **2017,** 29, (11), 4667-4674.
27. Brandt, R. E.; Stevanovic, V.; Ginley, D. S.; Buonassisi, T., Identifying defect-tolerant semiconductors with high minority-carrier lifetimes: beyond hybrid lead halide perovskites. *Mrs Communications* **2015,** 5, (2), 265-275.
28. Brandt, R. E.; Kurchin, R. C.; Hoye, R. L. Z.; Poindexter, J. R.; Wilson, M. W. B.; Sulekar, S.; Lenahan, F.; Yen, P. X. T.; Stevanovic, V.; Nino, J. C.; Bawendi, M. G.; Buonassisi, T., Investigation of Bismuth Triiodide (Bil(3)) for Photovoltaic Applications. *Journal of Physical Chemistry Letters* **2015,** 6, (21), 4297-4302.
29. Lehner, A. J.; Wang, H. B.; Fabini, D. H.; Liman, C. D.; Hebert, C. A.; Perry, E. E.; Wang, M.; Bazan, G. C.; Chabinyc, M. L.; Seshadri, R., Electronic structure and photovoltaic application of BiI3. *Applied Physics Letters* **2015,** 107, (13), 131109.
30. Han, H.; Hong, M.; Gokhale, S. S.; Sinnott, S. B.; Jordan, K.; Baciak, J. E.; Nino, J. C., Defect Engineering of BiI3 Single Crystals: Enhanced Electrical and Radiation Performance for Room Temperature Gamma-Ray Detection. *Journal of Physical Chemistry C* **2014,** 118, (6), 3244-3250.
31. DiPalma, J. R., Bismuth Toxicity, Often Mild, Can Result in Severe Poisonings. *Emergency Medicine News* **2001,** 23, (3).

32. Organization, W. H., Lead in Drinking-water. In *Background document for development of*
WHO Guidelines for Drinking-water Quality, World Health Organization: Online, 2011; p 26.
33. Futscher, M. H.; Ehrler, B., Efficiency Limit of Perovskite/Si Tandem Solar Cells. *Acs Energy Letters* **2016,** 1, (4), 863-868.
34. Hamdeh, U. H.; Nelson, R. D.; Ryan, B. J.; Bhattacharjee, U.; Petrich, J. W.; Panthani, M. G., Solution-Processed BiI3 Thin Films for Photovoltaic Applications: Improved Carrier Collection via Solvent Annealing. *Chemistry of Materials* **2016,** 28, (18), 6567-6574.
35. Norby, P.; Jorgensen, M. R. V.; Johnsen, S.; Iversen, B. B., Bismuth Iodide Hybrid Organic-Inorganic Crystal Structures and Utilization in Formation of Textured BiI3 Film. *European Journal of Inorganic Chemistry* **2016**, (9), 1389-1394.
36. Carmalt, C. J.; Clegg, W.; Elsegood, M. R. J.; Errington, R. J.; Havelock, J.; Lightfoot, P.; Norman, N. C.; Scott, A. J., Tetrahydrofuran adducts of bismuth trichloride and bismuth tribromide. *Inorganic Chemistry* **1996,** 35, (12), 3709-3712.
37. Miller, S.; Fanchini, G.; Lin, Y. Y.; Li, C.; Chen, C. W.; Su, W. F.; Chhowalla, M., Investigation of nanoscale morphological changes in organic photovoltaics during solvent vapor annealing. *Journal of Materials Chemistry* **2008,** 18, (3), 306-312.
38. Xiao, Z. G.; Dong, Q. F.; Bi, C.; Shao, Y. C.; Yuan, Y. B.; Huang, J. S., Solvent Annealing of Perovskite-Induced Crystal Growth for Photovoltaic-Device Efficiency Enhancement. *Advanced Materials* **2014,** 26, (37), 6503-6509.
39. Conboy, J. C.; Olson, E. J. C.; Adams, D. M.; Kerimo, J.; Zaban, A.; Gregg, B. A.; Barbara, P. F., Impact of solvent vapor annealing on the morphology and photophysics of molecular semiconductor thin films. *Journal of Physical Chemistry B* **1998,** 102, (23), 4516-4525.
40. Katahara, J. K.; Hillhouse, H. W., Quasi-Fermi level splitting and sub-bandgap absorptivity from semiconductor photoluminescence. *Journal of Applied Physics* **2014,** 116, (17), 173504.
41. Braly, I. L.; Hillhouse, H. W., Optoelectronic Quality and Stability of Hybrid Perovskites from MAPbI3 to MAPbI2Br Using Composition Spread Libraries. *The Journal of Physical Chemistry C* **2016,** 120, (2), 893-902.
42. Stoddard, R. J.; Eickemeyer, F. T.; Katahara, J. K.; Hillhouse, H. W., Correlation Between Photoluminescence and Carrier Transport and a Simple In-Situ Passivation Method for High-Bandgap Hybrid Perovskites. *The Journal of Physical Chemistry Letters* **2017**.
43. Levine, I.; Gupta, S.; Brenner, T. M.; Azulay, D.; Millo, O.; Hodes, G.; Cahen, D.; Balberg, I., Mobility–Lifetime Products in MAPbI3 Films. *The Journal of Physical Chemistry Letters* **2016,** 7, (24), 5219-5226.
44. Hutchinson, J. W., Stresses and failure modes in thin films and multilayers. *Notes for a Dcamm Course. Technical University of Denmark, Lyngby* **1996**, 1-45.
45. Gispert, J. R., Coordination Chemistry. In WILEY-VCH Verlag GmbH & Co. KGaA Weinham: Betz-Druck GmbH, Darmstadt, 2008; pp 199-236.
46. Pearson, R. G., Hard and Soft Acids and Bases. *Journal of the American Chemical Society* **1963,** 85, (22), 3533-3539.
47. Sanderson, J.; Bayse, C. A., The Lewis acidity of bismuth(III) halides: a DFT analysis. *Tetrahedron* **2008,** 64, (33), 7685-7689.
48. Kuech, T., Handbook of Crystal Growth: Thin Films and Epitaxy. In *Handbook of Crystal Growth*, Elsevier Science: 2014; pp 555-604.

49. Cuna, A.; Aguiar, I.; Gancharov, A.; Perez, M.; Fornaro, L., Correlation between growth orientation and growth temperature for bismuth tri-iodide films. *Crystal Research and Technology* **2004,** 39, (10), 899-905.
50. Zimmermann, E.; Wong, K. K.; Müller, M.; Hu, H.; Ehrenreich, P.; Kohlstädt, M.; Würfel, U.; Mastroianni, S.; Mathiazhagan, G.; Hinsch, A.; Gujar, T. P.; Thelakkat, M.; Pfadler, T.; Schmidt-Mende, L., Characterization of perovskite solar cells: Towards a reliable measurement protocol. *APL Materials* **2016,** 4, (9), 091901.
51. Li, Y. B.; Cooper, J. K.; Liu, W. J.; Sutter-Fella, C. M.; Amani, M.; Beeman, J. W.; Javey, A.; Ager, J. W.; Liu, Y.; Toma, F. M.; Sharp, I. D., Defective TiO2 with high photoconductive gain for efficient and stable planar heterojunction perovskite solar cells. *Nature Communications* **2016,** 7.
52. Nguyen, W. H.; Bailie, C. D.; Unger, E. L.; McGehee, M. D., Enhancing the Hole-Conductivity of Spiro-OMeTAD without Oxygen or Lithium Salts by Using Spiro(TFSI)(2) in Perovskite and Dye-Sensitized Solar Cells. *Journal of the American Chemical Society* **2014,** 136, (31), 10996-11001.
53. Chen, H. W.; Huang, T. Y.; Chang, T. H.; Sanehira, Y.; Kung, C. W.; Chu, C. W.; Ikegami, M.; Miyasaka, T.; Ho, K. C., Efficiency Enhancement of Hybrid Perovskite Solar Cells with MEH-PPV Hole-Transporting Layers. *Scientific Reports* **2016,** 6.

Appendix: Supplemental Information

Supplemental Information for

SOLUTION PROCESSED BiI_3 FILMS WITH 1 EV QUASI-FERMI LEVEL SPLITTING: ROLE OF WATER, TEMPERATURE, AND SOLVENT DURING PROCESSING

Titania Deposition:

TiO_2 solutions were prepared by mixing 10 mL ethanol (200 proof, Sigma-Aldrich), 69 µL HCl (37% wt., aq., Macron Fine Chemicals), and 0.727 mL Ti(IV)ethoxide (Aldrich) and mixing for 30 minutes at room temperature. Solution was prepared in air. The FTO substrates were cleaned with an Ar plasma for 10 minutes immediately before depositing the TiO_2. TiO_2 solution was dynamically spin coated on the FTO at 2,000 rpm for 15s. The solution is loaded into a plastic syringe with a 0.2 µm PTFE syringe filter. The FTO substrates are placed onto the spin coated and the spin coater is started. The first drop of solution is discarded. The substrate is then coated with four drops of solution. After all substrates are coated, the films were placed in a foil-covered petri dish and annealed in air with the following steps: 1) room temperature → 500°C over 50 minutes (~10°C/min ramp); 2) hold at 500°C for 30 minutes; 3) oven off, cooled overnight. The next day, the TiO_2 coated FTO was cleaned by sonication in 2-propanol, followed by a 10 minutes Ar plasma, followed by heating on a hotplate in air at 100°C for 10 minutes. After the hotplate heating step, the coating and annealing was repeated once more for a total of two layers of TiO_2. The twice-coated substrates were cleaned with 2-propanol and Ar plasma immediately before BiI_3 spin coating.

Film deposition and solvent vapor annealing:

BiI_3 was deposited on top of the TiO_2-coated substrates by applying two drops of the 200 mg/mL BiI_3 in THF + 1 vol.% DMSO from a syringe with an 0.2 µm PTFE filter. Films were spin coated at 2,000 rpm for 35s.

After spin coating, the BiI_3 films are solvent vapor annealed (SVA). The SVA setup (Figure S1) consists of three petri dishes. The cover of a smaller (~120 mL) petri dish is set inside the bottom of a larger petri dish. The petri dishes are preheated at the SVA temperature. One to four BiI_3 films

are placed in the center of the large petri dish along with a clean glass slide. After 60s, the SVA solvent is added to the glass slide. The films and solvent are now covered with the smaller petri dish. The whole setup is then covered by the top of the large petri dish. After nine minutes, the films are completely uncovered. They are dried in place for another 60s. The SVA temperatures reported here are the actual, measured surface temperatures.

Relative humidity calculations:

RH was calculated for the petri dish volume at each desired temperature according to the following procedure and equations:

a) Start with definition of RH (1) and rearrange to get (2). This gives us an expression for the partial pressure of water at a targeted RH.

b) Use the Antoine equation (3) and rearrange to get (4). This gives us an expression for the saturation pressure of water at a given temperature.

c) Start with the ideal gas equation (5) and rearrange to get (6). This gives us an expression for moles of water per volume for a given partial pressure of water.

d) Substitute (2) and (4) into (6) to get (7). We can now solve for moles of water per volume for a desired RH and T.

e) Multiply the result of (7) by the molecular weight of water to get mass of water per volume (8). This allows us to calculate the mass of water needed to give a desired RH at a given temperature, for a given volume.

$$(1)\ \mathrm{RH} = \frac{p_{\mathrm{water}}}{p_{\mathrm{sat,\,water}}}$$
$$(2)\ p_{\mathrm{water}} = \mathrm{RH} \times p_{\mathrm{sat,\,water}}$$
$$(3)\ \log_{10}(p_{\mathrm{sat,\,water}}) = A - \frac{B}{T+C}$$
$$(4)\ p_{\mathrm{sat,\,water}} = 10^{A-\frac{B}{T+C}}$$
$$(5)\ p_{\mathrm{water}} V = \mathrm{nRT}$$
$$(6)\ \frac{n}{V} = \frac{p_{\mathrm{water}}}{\mathrm{RT}}$$
$$(7)\ \frac{n}{V} = \mathrm{RH} \times 10^{A-\frac{B}{T+C}}$$
$$(8)\ \frac{\mathrm{mass\ of\ water}}{V} = \frac{n}{V} \times \mathrm{MW_{water}}$$

Equations 1-8. Relative Humidity Calculation

Closed-jar DMF SVA experiments:

We performed experiments with DMF SVA inside a closed jar. This avoids the gradual DMF escape that occurs when SVA is performed under petri dishes on a hotplate. Spin coated films were loaded into jars with a small amount of DMF and sealed. These jars were then placed in an oven preheated to 100°C. All films treated this way turned orange, resulting in the large, needle like morphologies seen in Figure S6.

Van't Hoff theory:

The complexation between DMF and BiI_3 is given by $4\,BiI_3 + 8\,DMF \leftrightarrow [Bi(DMF)_8]^{3+}[Bi_3I_{12}]^{3-}$. We can then write an expression for the equilibrium constant as:

$$K_{eq}(T) = \frac{a_1[[Bi(DMF)_8]^{3+}[Bi_3I_{12}]^{3-}]}{(a_2[BiI_3])^4(\,a_3[DMF])^8}$$

Where a_i is the activity of a component. Activities of solids are 1 by definition. Activities of ideal gases are given as the ratio of the gas partial pressure to the standard pressure. Rewriting our expression for K_{eq}:

$$K_{eq}(T) = \frac{1}{\left(\frac{p[DMF]}{p_0}\right)^8}$$

Using the ideal gas law, we can get an expression for p in terms of number of moles of DMF, temperature and volume. Now, consider the Van't Hoff equation:

$$ln\left(K_{eq}(T)\right) = -\frac{\Delta H}{R\,T} + \frac{\Delta S}{R}$$

Using our expression for K_{eq} and the Van't Hoff equation, we can plot $\ln(K_{eq})$ as a function of 1/T. In doing this, we can extract ΔH and ΔS.

Photoluminescence measurement:

AIPL measured at one sun photon flux (1.28×10^{21} photons/s-m^2 for 1.8 eV band gap material illuminated with a 532 nm laser) is the most device relevant photoluminescence measurement. However, measuring AIPL at one sun for BiI_3 is a challenge due to low PLQY. In our typical setup, a 532 laser is focused through a 10x Olympus objective, giving a ~ 12 μm diameter spot on the sample. With this small spot size, we cannot collect signal at one sun injection. Increasing the area over which we excite the sample is a way to increase signal. To achieve this, we increase the laser spot size by placing a defocusing lens in the beam path. After passing through the lens and the 10x objective, the spot size is now ~ 170 μm in diameter as determined by a beam profiler. The defocused laser also overfills the objective, so the beam profile is now more square shaped, rather than being a typical Gaussian. The laser power is then adjusted to match the appropriate one sun flux. With this larger spot size, collecting AIPL at one sun is now possible.

Two-point lateral DC photoconductivity theory:

We can measure σ_{ph}, the lateral DC photoconductivity as:

$$\sigma_{ph} = \sigma_l - \sigma_d$$

Where σ_l and σ_d are the light and dark conductivities respectively. A BiI_3 film is illuminated with a known above band gap flux and biased between two contact pads with known dimensions and separation. The current is then measured. A relative diffusion length can then be calculated as:

$$L_D = \sqrt{\sigma_{ph} kT / 2q^2 G}$$

q and G are the elementary charge and average volumetric photogeneration rate. It is important to note that the diffusion length measured here is not an electron or hole diffusion length. Rather, it is indication of the relative diffusive transport in a film. See Stoddard et al.[1] for full details and derivation of equations.

Figure S1. Representation of the SVA setup. The BiI_3 film and SVA solvent are covered by a smaller petri dish inside a larger petri dish. This helps protect the films from large temperature variations or drafts during SVA. The temperatures used are the actual (measured) temperatures of the inside of the petri dish and not the setpoint of the hotplate.

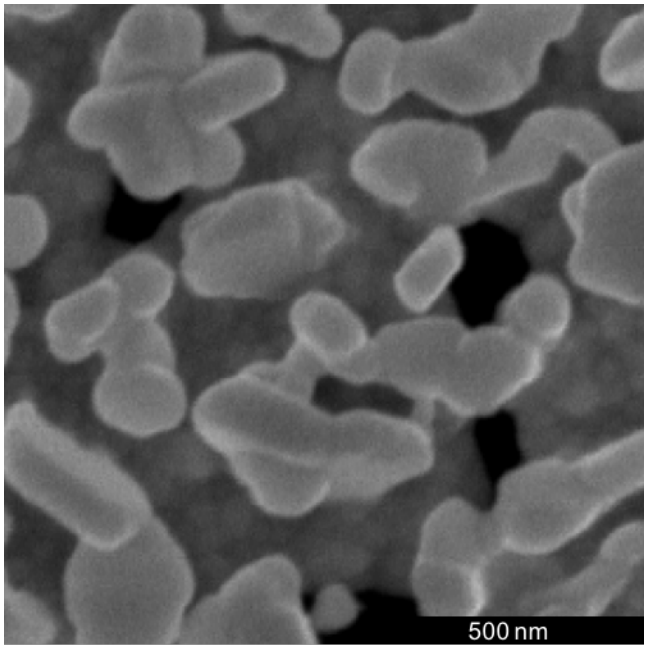

Figure S2. SEM image of BiI_3film on FTO/TiO_2 prepared from a 200 mg/mL BiI_2 in THF + 2% vol. DMF ink

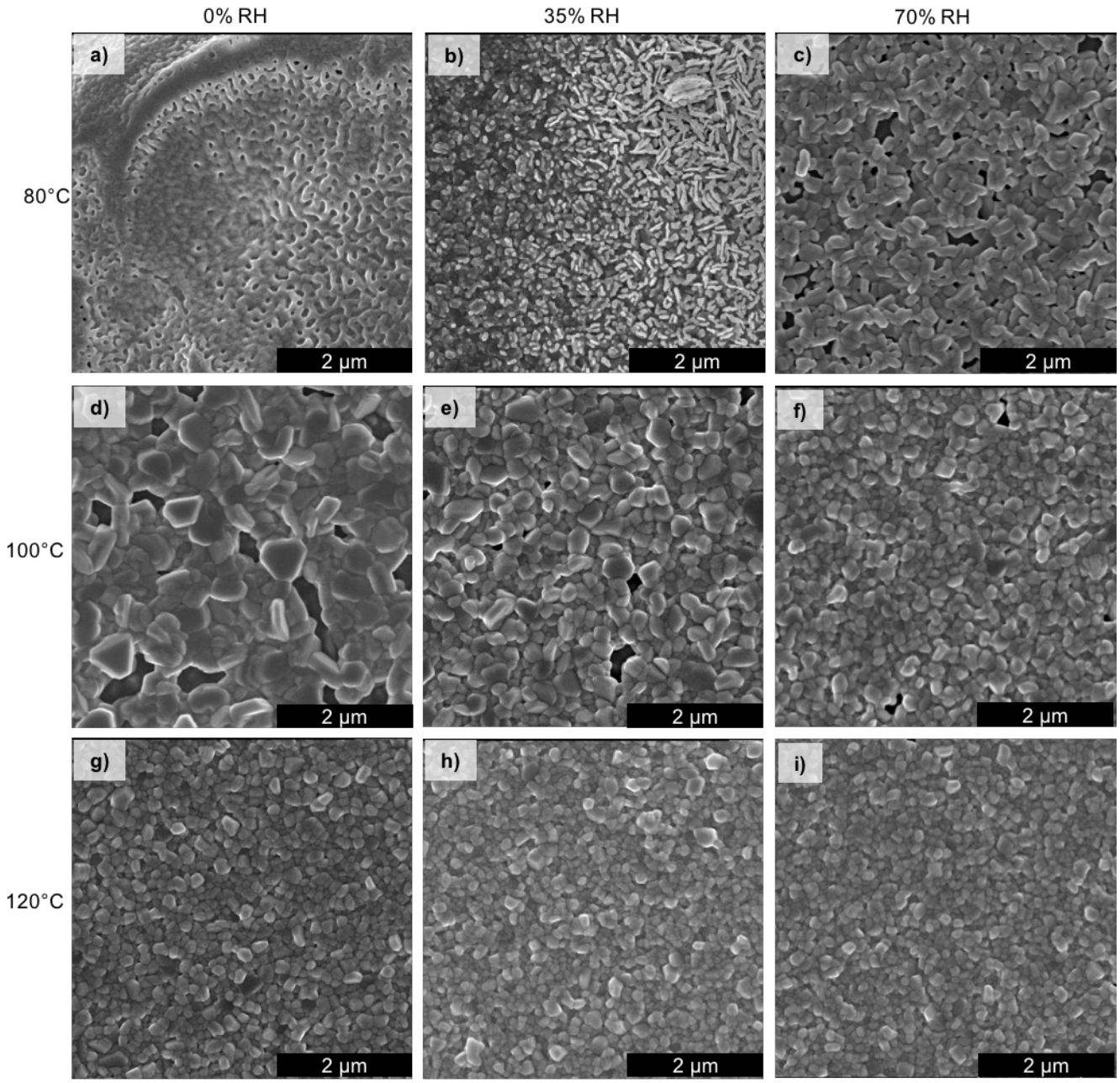

Figure S3. SEM images of glove box films after SVA under the following conditions: a) 80°C and 0% RH, b) 80°C and 35% RH, c) 80°C and 70% RH, d) 100°C and 0% RH, e) 100°C and 35% RH, f) 100°C and 70% RH, g) 120°C and 0% RH, h) 120°C and 35% RH, and i) 120°C and 70% RH. The RH values are calculated with respect to the SVA temperature.

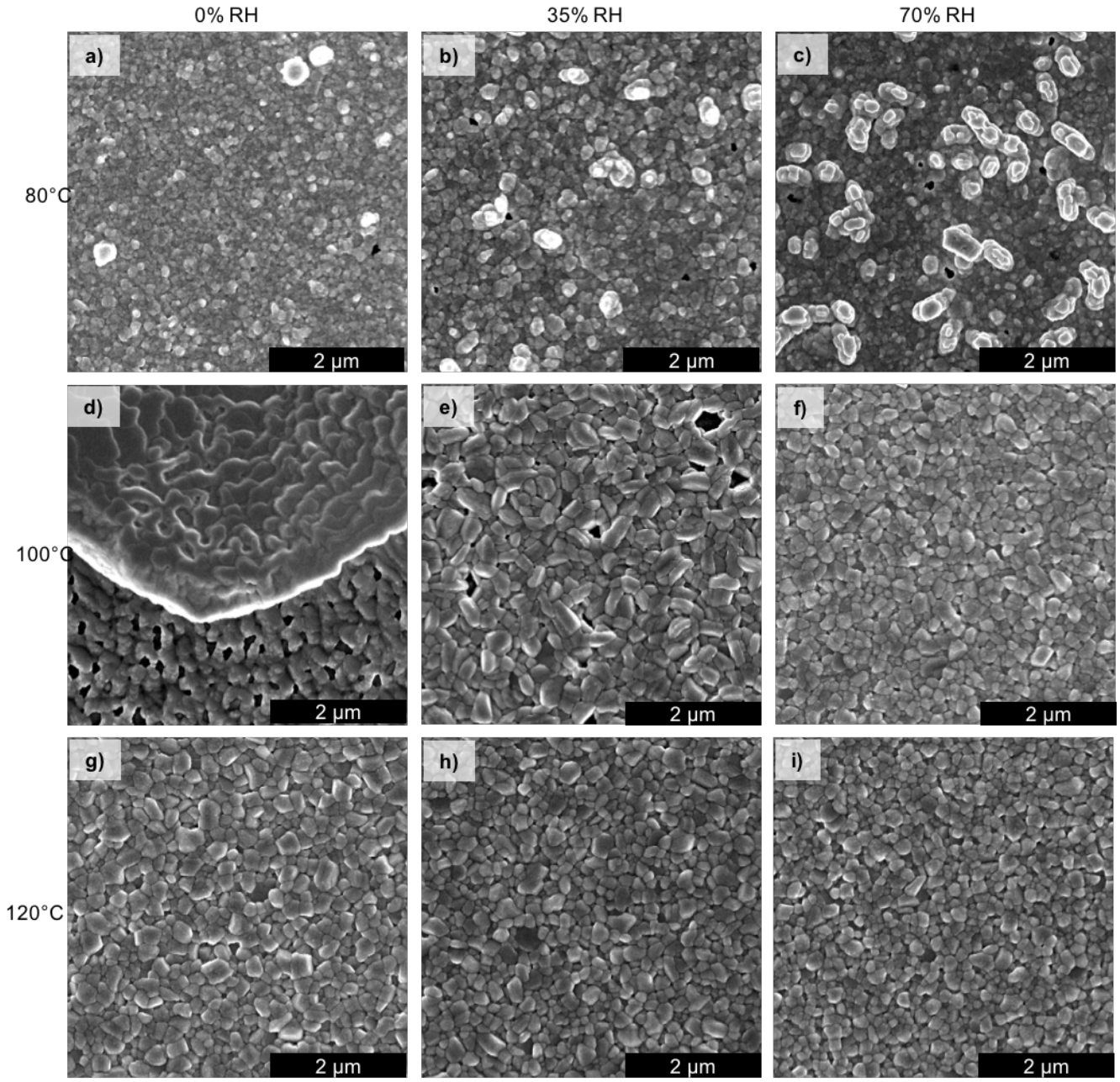

Figure S4: SEM images of fume hood films after SVA under the following conditions: a) 80°C and 0% RH, b) 80°C and 35% RH, c) 80°C and 70% RH, d) 100°C and 0% RH, e) 100°C and 35% RH, f) 100°C and 70% RH, g) 120°C and 0% RH, h) 120°C and 35% RH, and i) 120°C and 70% RH. The RH values are calculated with respect to the SVA temperature.

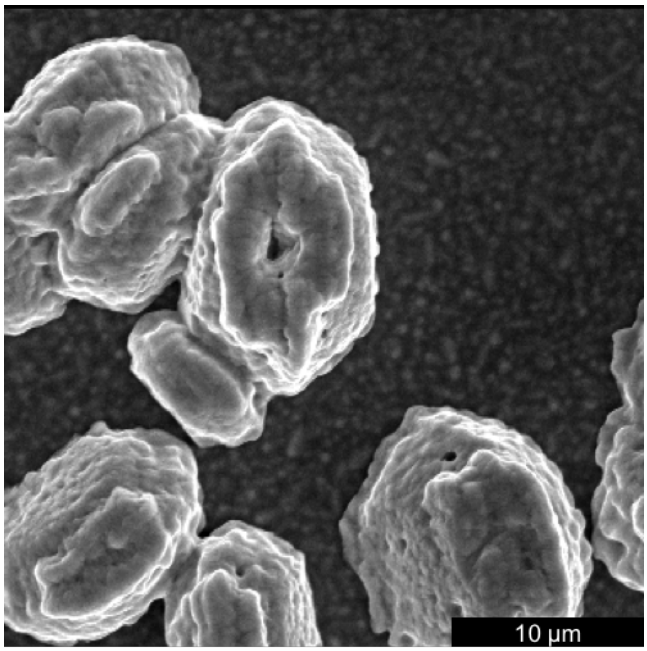

Figure S5. SEM image of BiI_3 film on FTO/TiO_2 treated with glove box DMSO SVA at 100°C.

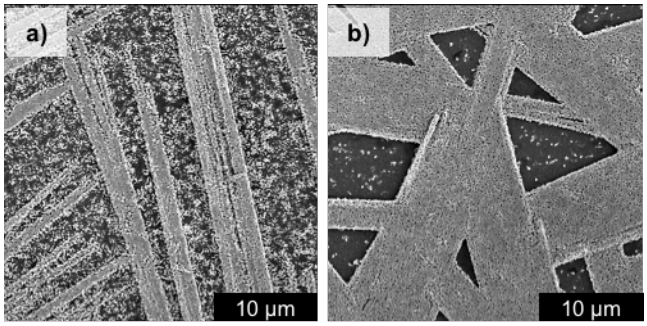

Figure S6. SEM image of BiI_3 films grown on FTO/TiO in air_2 treated with DMF SVA in a closed jar at 100°C with a) 20µL DMF for 20 minutes and b) 5µL DMF for 5 minutes.

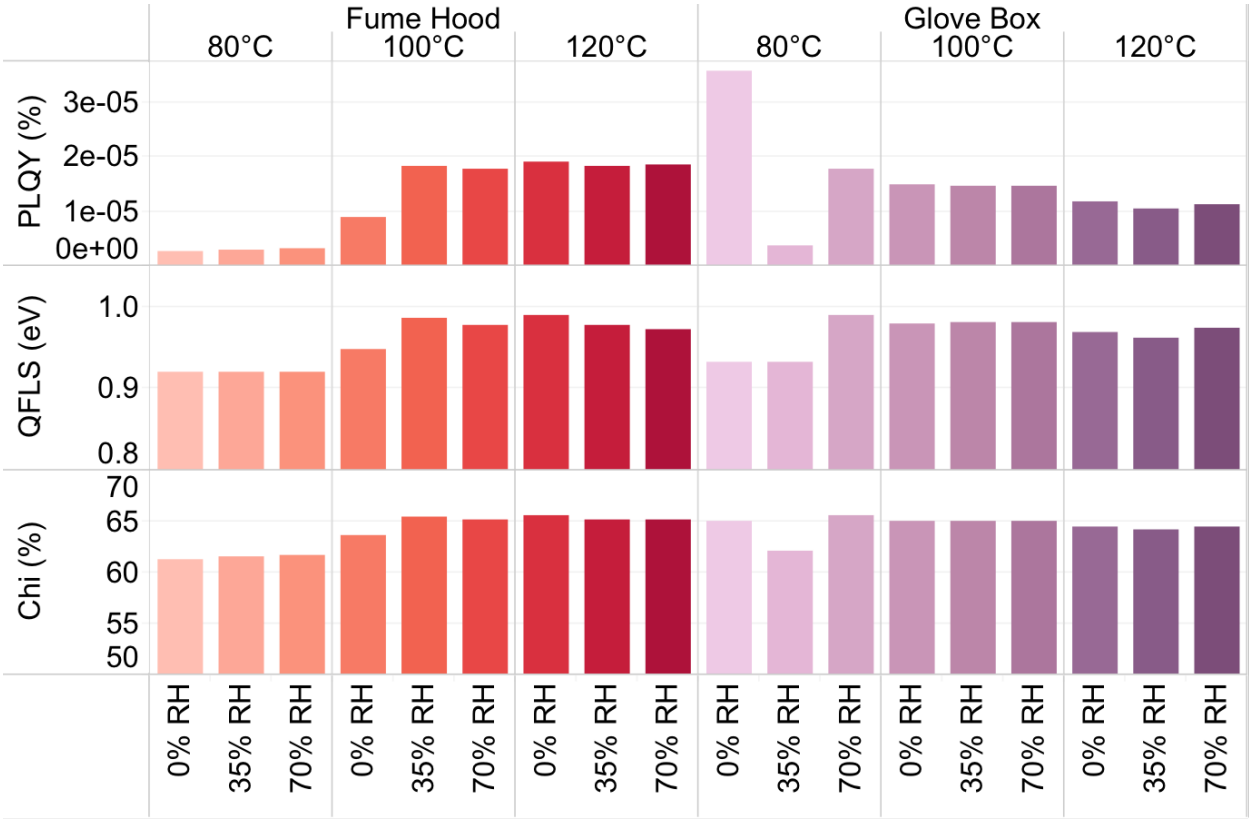

Figure S7. Full PLQY, QFLS, and Chi results of BiI_3 films for the temperature, humidity, and environment experimental series. Red data is from films prepared in air. Purple data is from films prepared in the glove box.

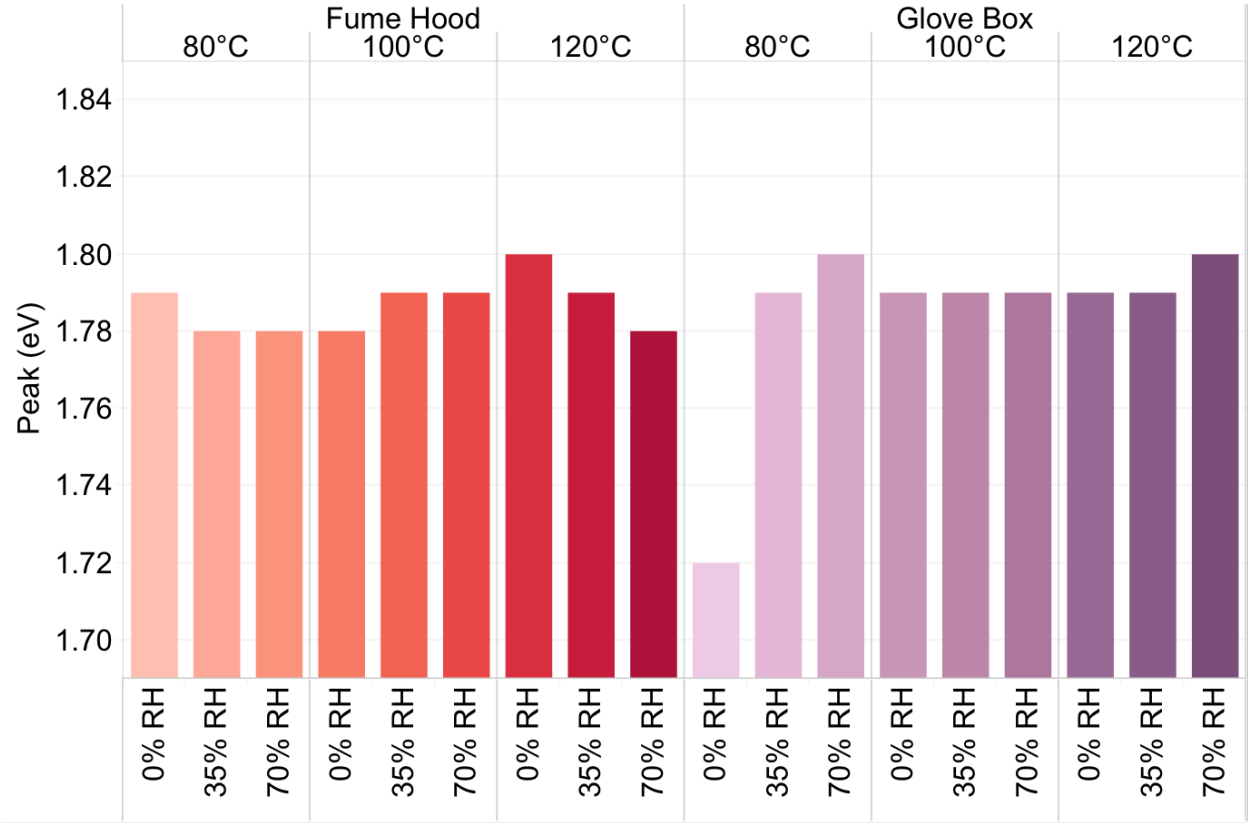

Figure S8. Full peak position results of BiI_3 films for the temperature, humidity, and environment experimental series. Red data is from films prepared in air. Purple data is from films prepared in the glove box.

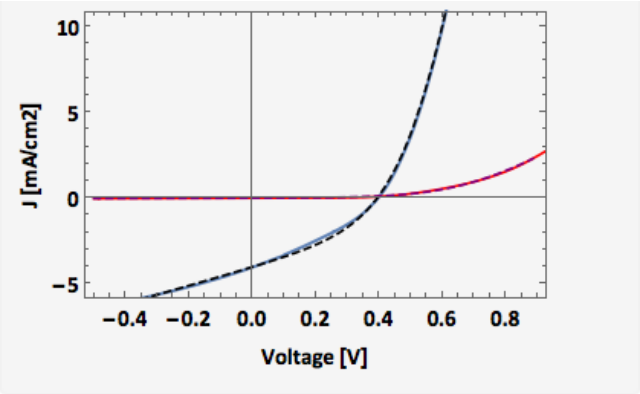

Figure S9. LambertW fitting of non-deal diode equation of JV data from device made at 120 °C and 70% RH. Red trace is dark curve, blue trace is illuminated curve. Dashed lines indicate fits.

1. Stoddard, R. J.; Eickemeyer, F. T.; Katahara, J. K.; Hillhouse, H. W., Correlation Between Photoluminescence and Carrier Transport and a Simple In-Situ Passivation Method for High-Bandgap Hybrid Perovskites. *The Journal of Physical Chemistry Letters* **2017**.